RUHR UNIVERSITÄT BOCHUM RUB

DLR Deutsches Zentrum für Luft- und Raumfahrt German Aerospace Center

Characterization of an Acetylene-Oxygen Flame for Material Studies on High-Temperature Materials

by

Melih Aydin

108017260901

Master's thesis

submitted in partial fulfillment of the requirements
for the degree of Master of Science in Computational Engineering

Department of Civil and Environmental Engineering
Ruhr University Bochum

August 2020

Supervisors: Prof. Dr. rer. nat. Klaus Hackl
Institute of Mechanics of Materials
Ruhr University Bochum

Dipl.-Ing. Thomas Reimer
Dr. Giuseppe Di Martino
Institute of Structures and Design
German Aerospace Center

Declaration

Hereby I declare, that I have not submitted this thesis in this or similar form to any other examination at the Ruhr-University Bochum or any other Institution of High School.

I officially ensure, that this paper has been written solely on my own. I herewith officially ensure, that I have not used any other sources but those stated by me. Any and every parts of the text which constitute quotes in original wording or in its essence have been explicitly referred by me by using official marking and proper quotation. This is also valid for used drafts, pictures and similar formats.

I also officially ensure, that the printed version as submitted by me fully confirms with my digital version. I agree that the digital version will be used to subject the paper to plagiarism examination.

Abstract

Many experiment methods are possible for assessing the high-temperature performance of high-temperature materials, e.g., laser ablation testing, oxyacetylene torch testing, plasma wind tunnel testing, strip heater testing and scramjet testing. Oxyacetylene torch testing is the fast and economical method to assess the high-temperature performance of materials. In this regards, at the DLR Institute of Structures and Design, an oxyacetylene torch-testing facility has been established to perform high-temperature oxidation testing of UHTC materials such as CCSiC and UHT-CMC at temperatures up to about 2000 K. The purpose of the present work is to characterize the oxyacetylene burner flame and followingly, to make a statement about the thermal behaviours of the aforementioned materials in terms of heat flux incident and the related temperature fields. The results verified numerically and experimentally will then lead to supervise the experimental facility efficiency.

Acknowledgement

The project is a vision of Deutsche Zentrum für Luft- und Raumfahrt and I am thankful to them to consider myself as a very lucky individual as I was provided with an opportunity to be a part of this project and work on it as my thesis. It was a great chance for learning and professional development. I greatly appreciate the freedom they provided me to explore new ideas with their kind supports and also the necessary guidance concerning projects implementation.

I thank my thesis supervisor Dipl.-Ing.Thomas Reimer for providing invaluable guidance throughout my thesis. His door to the office was always open whenever I ran into a trouble spot or had a question about my research or writing. I am thankful for all his aspiring guidance, invaluably constructive criticism and friendly advice during the project work.

I express my warm thanks and deep gratitude to Dr.Giuseppe Di Martino for his incessant support and guidance at DLR. His expertise, experience and technical support served as the backbone in the implementation.

Finally, I wish to thank my esteemed professor Prof.Dr.rer.nat.Klaus Hackl to become my thesis supervisor. His kind supports and inspiring motivation was the core factor to accomplish the master thesis.

List of Figures

List of Tables

Table of Contents

Chapter 1

Introduction

At the DLR Institute of Structures and Design, a burner facility was installed, using the oxyacetylene for carrying out high-temperature material tests. As it is a well-known fact that hypersonic and atmospheric re-entry vehicles experience temperatures over $2000K$ and encounter corrosive plasmas from the atmosphere at high speeds. The materials used in these vehicles, especially at the sharp edges, should maintain their shape under this severe oxidation, extreme heat fluxes and high mechanical stress conditions [1]. In this regard, material samples from the area of the heat shields for spacecraft, such as carbon fibre reinforced silicon carbide matrix composite (CCSiC) and ultra-high temperature ceramic matrix composites (UHT-CMC), are to be exposed to high temperatures in an oxidative environment to be able to make a statement about the oxidation behaviour in future studies [1][2][3]. An example of a possible use case was investigated with the CCSiC material as the structure of the nozzle extension of a scramjet engine tested at NASA Langley by Glass et al. [4].

The numerical simulations for the experimental facility will be examined in this study. The field of Computational Fluid Dynamics, abbreviated as CFD, is a very famous application area for providing solutions for fluid flows with or without solid interaction [5]. Combustion is one of the fields where CFD is applied. To simulate combustion accurately, the theories linked with the fluid dynamics and combustion chemistry must be known properly. All the transport phenomena such as convection and diffusion as well as the additional transport equations, such as turbulent and species transport equations including chemical reaction mechanisms should be meticulously included in the model to estimate the formation of combustion products, species and structure of the flame. While doing that, the reaction

models, such as the eddy dissipation model and eddy dissipation concept model, should be investigated and the one gives better solution should be selected. To understand whether the flame is correctly characterized, the concentrations of the species in the flame shall be assessed.

In the following, the conjugate heat transfer which estimates the heat transfer between the oxyacetylene flame and the materials due to thermal contact shall be conducted. The thermal evaluations will be done based on the temperature field and the overall heat flux on the materials. The thermal studies on the materials lead to determine a design for suitable experiment setup and sample holders, which are water-cooled copper holder ($295K$ water cooling at backside) and graphite holder, for material tests.

Chapter 2

Theory

For all flows, ANSYS Fluent solves Navier-Stokes equations which consist of conservation equations for mass and momentum [6]. For flows including heat transfer, species mixing or reactions, the energy conservation equation is solved. Moreover, additional transport equations are also required in case the flow is turbulent. To characterize the acetylene-oxygen burner flame all equations emphasized above should be evaluated and generated.

2.1 Navier-Stokes Equations

The equations were derived independently by G.G. Stokes, in England, and M. Navier, in France, in the early 1800s [6][7]. The Navier-Stokes equations apart from additional transport equations and species conservation equations which then be added in this study, consist of a time-dependent continuity equation for conservation of mass, three time-dependent conservation of momentum equations and time-dependent conservation of energy equation [7].So, to solve a simple flow problem, all five equations and six unknowns are needed to be solved simultaneously. That is why these are commonly called as a coupled system of equations.

2.1.1 Reynolds-Averaged Navier–Stokes Equations

There are three types of model which are Direct Numerical Simulation(DNS), Large Eddy Simulation(LES) and Reynolds Averaged Numerical Simulation (RANS) to solve Navier-Stokes equations in the case of turbulent flows.

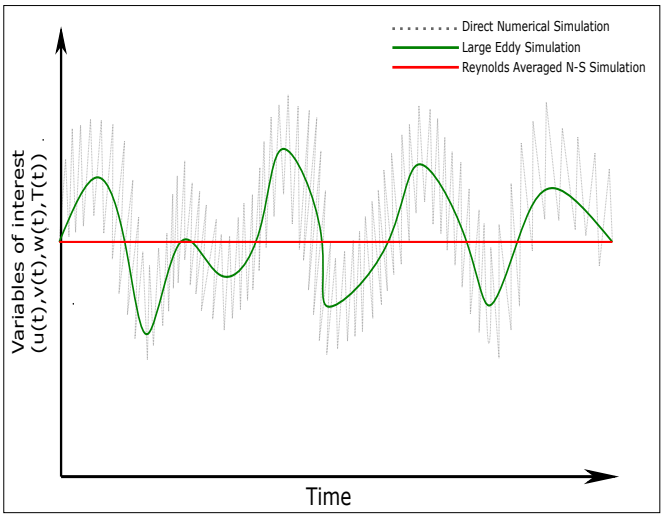

Figure 2.1: Comparision of the solution between three models

The Figure 2.1 depicts the flow quantities taken from a very small time scale. As it is seen, DNS simulations are the most accurate model since it covers all flow phenomena accurately. However, the computational time is a big optimization problem in the industry and in this regard, DNS is not being used for most Computational Fluid Dynamics (CFD) applications. Therefore, RANS, called time-averaged simulation model, is widely used due to being less time-consuming, less need for computational power and providing acceptable solutions in most industrial applications. The definition of the time-averaged means any variable (like velocity, pressure or temperature etc.) of the equation decomposed into the mean (time-averaged) component ($\bar{u}$) and the fluctuating component (u') at a specific point [8]. Afterwards, these decomposed variables are added into Navier-Stokes equations.

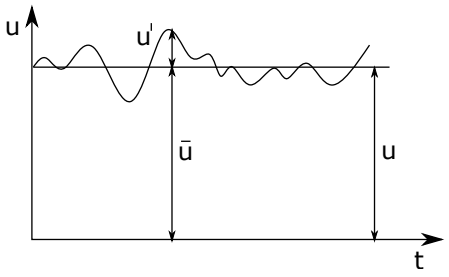

Figure 2.2: RANS decomposition

Hence, the accuracy of the CFD simulation which RANS model has been applied is mainly determined by the mesh resolution and the turbulence model.

2.1.2 Discretization

The spatial discretization of the domain is necessary to apply in the solution domain. So, the considered domain divided into finite elements. In theory, there are three methods of discretization: [9]

- Finite difference method
- Finite volume method
- Finite element method

The method used in Ansys Fluent is the cell-centred Finite Volume Method (FVM). The FVM is used due to its good accuracy and flexibility in CFD applications. The cell-centred means that each flow variables to be solved are only stored at the cell-centre of each cell [10].

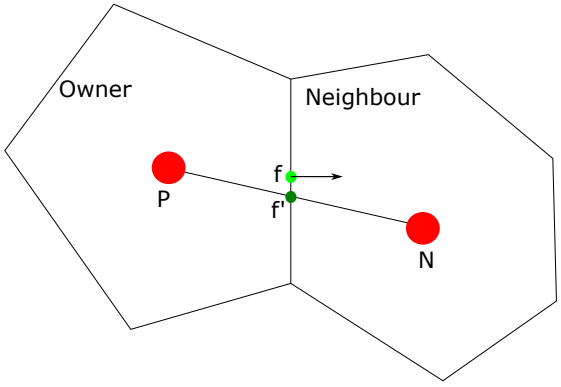

Figure 2.3: The cell-centered elements

As it is seen in Figure 2.3, the flow variables at the cell centres are known parameters. however although the cell-centre values of the different variables are the quantities of main interest, face-centre values are also needed for the evaluation of the convective terms of the Navier-Stokes equations. To compute these variables, the interpolation schemes should be applied. There are few interpolation schemes however the first-order and the second-order upwind schemes are commonly used. The first order schemes are less accurate but more stable due to setting the face value,ϕ_f, equal to the cell-centre value,ϕ, in the upstream cell. However, the second-order schemes which are more accurate compute cell face quantities by applying a multidimensional linear reconstruction which uses a Taylor series expansion to

achieve high-order accuracy. The face value, ϕ_f, is computed using the following expression:

$$\phi_f = \phi + \nabla\phi \cdot \vec{r} \tag{2.1}$$

where ϕ and $\nabla\phi$ are the cell-centered value and its gradient in the upstream cell and $\vec{(r)}$ is the distance from the upstream centroid to the face centroid [10]. The gradient $\nabla\phi$ is determined by the least-squares cell-based method where the solution is assumed to vary linearly.

It is clear in Figure 2.3 that any average value defined at P and N will be interpolated at $f^{'}$ rather than f, the actual centre point of the face [10]. Thus any unstructured discretization using this interpolated value will not have a zero accuracy. However, the accuracy might be increased by good quality mesh. The mesh metrics for CFD application might be judged by taking into account mesh orthogonality, skewness and aspect ratios. Mesh orthogonality which determines the angle between cell centre and face centre can be defined as the most important parameter for cell-centred FVM. The smaller angle will provide more accurate interpolated results.

2.1.2.1 Mesh Types

There are two basic types of mesh creation:

- Block-structured mesh
- Unstructered mesh

The basic difference between these mesh types is the connectivity of the elements. Each element has the same number of neighbouring elements in block-structured mesh whereas the number of neighbouring cells can vary in the unstructured mesh. In this study, the quad-dominant unstructured mesh will be generated due to providing flexibility and higher quality to create finer grids in the regions where the large gradients exist. Furthermore, quad-dominant unstructured mesh provides good quality mesh in terms of orthogonality that reduces computational time while enabling users to generate smooth transition with triangle elements in the transition region between refined and coarse mesh zones.

2.1.3 Turbulence Model

Several turbulence models are being used in CFD applications. However, *the SST k-omega* turbulence model called a two-equation eddy-viscosity model will be applied in this study. It is a hybrid model combining the Wilcox k-omega near the wall and the k-

epsilon models in the free stream [11]. This assures that the model is used with appropriate turbulence resolution throughout the flow field due to being well suited in the viscous sub-layer and the regions composed of the flow separations. Thus, compared to the k-epsilon model which is another popular model, to perform high resolution in flow separations is the distinctive feature of this model.

2.1.4 Near-Wall Treatment

As it is depicted in Figure 2.4, the velocity presents a high gradient near the walls since it has to change from the free-stream value to 0. Similarly, also the temperature can fastly alter near the wall to reach the same value as the solid material. Consequently, it is of fundamental importance to numerically capture the aforementioned gradients since this determines the accuracy of the shear stresses and heat fluxes.

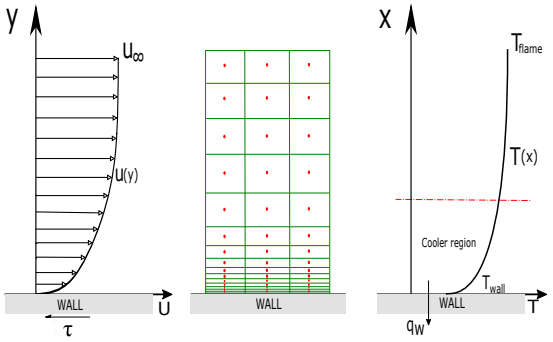

Figure 2.4: Near-wall treatment

Hence, the most common way to treat wall boundaries is meshing near-wall region finer so that the gradient of flow will be captured properly. Generally, combustion simulations require too much computational cost. At that point optimization becomes important. Therefore while saving computational time, accuracy should not be decreased. One of the important optimization parameters is dimensionless wall distance (y^+).

$$y^+ = \frac{u^* \cdot y}{\nu} \tag{2.2}$$

In the Equation 2.2, u^*, y, and ν are the friction velocity at the nearest wall, the distance to the nearest wall, the local kinematic viscosity of the fluid respectively. In case transitional flow, flow separations, heat transfer etc. are needed to be captured, the first cell has to be within the viscous sub-layer and the y^+ should be less than 1 [12].

2.2 Energy Equation

The energy equation is primarily being used to solve chemical reactions, the temperature fields in solution domains, and the conjugate heat transfer between physically different solution domains such as the fluid and the solid zone. The energy equation has the form:

$$\frac{\partial(\rho E)}{\partial t} + \nabla \cdot [\mathbf{U}(\rho E + p)] = \nabla \cdot \left[k_{\text{eff}} \nabla T - \sum_j h_j \mathbf{J}_j + \tau_{\text{eff}} \cdot \mathbf{U} \right] + S_h (2.3)$$

where k_{eff} is the effective conductivity and $\mathbf{J}_j$ is the diffusion flux of species j. The first three terms on the right-hand side of Equation 2.3 represent energy transfer due to *conduction*, *species diffusion*, and *viscous dissipation*, respectively [13]. S_h , called enthalpy sources, includes the heat of chemical reaction and any other volumetric heat sources which are defined.

The energy transport equation 2.3 has the total energy term(Equation 2.4) which consists of internal/thermal energy, kinetic energy, and pressure work as below.

$$E = h - \frac{p}{\rho} + \frac{v^2}{2} \tag{2.4}$$

The pressure work and the kinetic energy components of the total energy can be negligible for incompressible flows since their energy work is too small compared to internal/thermal energy which is represented by sensible enthalpy(Equation 2.5) [13]. In this work, the flow is evaluated as incompressible. However, in case of having a high-velocity field in the solution domain such as in supersonic flows the total energy should be considered with all components.

After simplification due to the assumption of incompressible flow, the total energy will be equal to the sensible enthalpy:

$$h = \sum_j Y_j h_j \tag{2.5}$$

where Y_j is the mass fraction of species j and h_j. The h_j is

$$h_j = \int_{T_{\text{ref}}}^{T} c_{p,j} dT \tag{2.6}$$

where cp_j is the specific heat transfer coefficient.

In the solid region, the velocity (U) is assumed to be zero and the energy equation is solved without velocity contribution inside. Then the energy equation in the solid region has the form:

$$\frac{\partial}{\partial t}(\rho h) = \nabla \cdot (k \nabla T) + S_h \tag{2.7}$$

where

- ρ is the density
- $\vec{v}$ is the the velocity

  field due to rotational or translational motion of the solids
- h is the sensible enthalpy (Equation 2.5)
- κ is the thermal conductivity
- T is the temperature
- S_h is the wolumetric heat source

2.2.1 Viscous Dissipation

It is also called viscous heating. This term should be considered in cases viscous shear in the fluid is large such as supersonic flow in rocket mechanics generating a high-velocity field in the head leading to the large heat effect and when the density-based solver is being used. To measure the importance of the viscous heating relative to the conductive heat transfer, the Brinkman number(Equation 2.8) can be investigated. There are various combinations for the Brinkman number however one is:

$$\mathrm{Br} = \frac{\mu u^2}{\kappa \left(T_w - T_0\right)} \tag{2.8}$$

where

- μ is the dynamic viscosity
- U is the flow velocity
- κ is the thermal conductivity
- T_w is the wall temperature
- T_0 is the bulk fluid temperature

In this study, the heat transfer region is in the location where the flow velocity is almost close to zero, also called the stagnation point. So, the viscous heating effect is negligible.

2.2.2 Species Diffusion

This term involves the effect of enthalpy transport due to species diffusion. It can be disabled in the pressure-based solver whereas the density-based solver always has this term in the energy equation to be solved. This term is automatically disabled in Ansys Fluent when the solver is pressure-based.

2.2.3 The Enthalpy Sources

The enthalpy is not the only term included inside the total energy but the term is also added to the right-hand side as the additional sources (Equation 2.9) since the content of the fluid flow can change in response to the chemical reaction.

$$S_{h,\mathrm{rxn}} = -\sum_{j} \left(\frac{h_j^0}{M_j} + \int_{T_{\mathrm{ref},j}}^{T} c_{p,j} dT \right) \mathcal{R}_j \tag{2.9}$$

The equation 2.9 represents the sources of energy due to the chemical reaction where h_j^0 is the enthalpy of formation of species j and $\mathcal{R}_j$ is the volumetric rate of creation of species j which is calculated with reaction models [13].

2.3 Combustion Model

Hydrocarbon combustion is related to the chemical reaction in which a hydrocarbon reacts with oxygen to produce carbon dioxide, water and then heat. To simulate combustion accurately, the theories linked with flow equations, energy equation and combustion chemistry must be known properly. All the additional transport equations such as turbulence and chemical kinetics which plays a significant role to estimate the formation of combustion products and species should be meticulously included in the model.

In acetylene-oxygen modelling, the simple one-step (global) chemical reaction or simplified (reduced) chemical reaction mechanisms which consist of more reactants/products and/or several reaction steps can be used to generate the flame. However, the reduced chemical reaction mechanisms are highly recommended due to providing the most accurate results relatively.

2.3.1 Single-Step Reaction Mechanism

Single-step global acetylene-oxygen reaction (Equation 2.10) can be written as:

$$2C_2H_2 + 5O_2 \rightarrow 4CO_2 + 2H_2O + Heat \tag{2.10}$$

However, it can not provide the appropriate resolution because, in reality, combustion occurs with more reactions and species than single-step global reaction has. The Arrhenius Equation (2.11) can easily prove why the global mechanism is not sufficient.

$$R_k = A \cdot (T^{\beta_r}) \cdot (e^{-\frac{E_r}{RT}}) \tag{2.11}$$

The Arrhenius equation(Equation 2.11), a formula for the temperature dependence of a chemical reaction rate consists of the Arrhenius reaction rate (A=$3.655 \cdot 10^{10}$), the activation energy ($E = 1.256 \cdot 10^8\ J/kgmol$) for the oxyacetylene reaction and the universal gas constant ($R = 8313\ J/kgmolK$) and the temperature (T) [14]. As an example, assume that turbulent flow at a specific point has constant species concentration and the temperatures vary as below.

Table 2.1: Reaction rates at different temperatures

T(K)	Reaction Rates(R_k)
300	$4.9 \cdot 10^{-12}$
1000	$1.0 \cdot 10^4$
1700	$5.0 \cdot 10^6$

It is clear that the average reaction rate ($\bar{R}_k$) is not equal to the reaction rate at the average temperature ($R_k(\bar{T})$) of all time. It proves that combustion systems need a special and extended-Arrhenius reaction models to overcome the disadvantages of using average temperature and constant Arrhenius reaction rate in combustion simulations.

2.3.2 Simplified Reaction Mechanisms

Single-step reaction mechanism with more products:

The single-step reaction mechanism can be extended with more products as,

$$C_2H_2 + \frac{5}{2}O_2 = \sum_i \omega_i X_i \tag{2.12}$$

where X_i is the species ($CO, CO_2, H, H_2, H_2O, O, O_2$ and OH) and the coefficients ω_i. The coefficients in Table 2.2 are determined on the basis of the chemical equilibrium composition at stoichiometric condition calculated with the NASA Computer program CEA (Chemical Equilibrium with Applications) which calculates properties of complex mixtures [15].

Table 2.2: Stoichiometric coefficients determined by NASA CEA program

Stoichiometric coefficients			
C_2H_2	1	H_2	0.161
O_2	2.5	H_2O	0.452
CO	1.4818	O	0.5024
CO_2	0.5182	OH	0.4326
H	0.3414	O_2	0.5474

The reaction and rate parameters for this one-step reaction mechanism is given in the Table 2.3. The pre-exponential factor (A) and activation energy (E_a) are Ansys Fluent default constants.

Table 2.3: Parameters for quasi reaction mechanisms

Fuel	A	Ea	a	b
C2H2	3.655×10^{10}	26.11	0.5	1.25

Multi-step detailed reaction mechanisms:

A more detailed mechanism for the combustion of the most common hydrocarbons has been reported and validated in [16]. In particular, it includes the first reaction between the hydrocarbon and the oxygen to produce CO and H_2, which in the general case for n-paraffin can be written in the form:

$$\mathrm{C}_n\mathrm{H}_{2m} + \frac{n}{2}\mathrm{O}_2 = n\mathrm{CO} + m\mathrm{H}_2 \tag{2.13}$$

The reaction and rate parameter for this reaction in the case of acetylene are given in the Table 2.4

Table 2.4: Parameters for quasi reaction mechanisms

Fuel	A	Ea	a	b
C2H2	1.2×10^{13}	30	0.5	1.25

This global reaction will be combined with 21 elementary reactions involving the $H_2 - O_2 - CO$ mechanism. This additional mechanism consists of 12 species. The reactions and rate parameters for the $H_2 - O_2 - CO$ mechanism are given in Table 2.5

Table 2.5: Reaction mechanism used in quasi-global mechanism for $\mathrm{CO} - \mathrm{H_2} - \mathrm{O_2}$ system

Reaction	A	n	E_a
$\mathrm{H} + \mathrm{O_2} = \mathrm{O} + \mathrm{OH}$	2.2×10^{14}	0.0	16.8
$\mathrm{H_2} + \mathrm{O} = \mathrm{H} + \mathrm{OH}$	1.8×10^{10}	1.0	8.9
$\mathrm{O} + \mathrm{H_2O} = \mathrm{OH} + \mathrm{OH}$	6.8×10^{13}	0.0	18.4
$\mathrm{OH} + \mathrm{H_2} = \mathrm{H} + \mathrm{H_2O}$	2.2×10^{13}	0.0	5.1
$\mathrm{H} + \mathrm{O_2} + M = \mathrm{HO_2} + M$	1.5×10^{15}	0.0	-1.0
$\mathrm{O} + \mathrm{HO_2} = \mathrm{O_2} + \mathrm{OH}$	5.0×10^{13}	0.0	1.0
$\mathrm{H} + \mathrm{HO_2} = \mathrm{OH} + \mathrm{OH}$	2.5×10^{14}	0.0	1.9
$\mathrm{H} + \mathrm{HO_2} = \mathrm{H_2} + \mathrm{O_2}$	2.5×10^{13}	0.0	0.7
$\mathrm{OH} + \mathrm{HO_2} = \mathrm{H_2O} + \mathrm{O_2}$	5.0×10^{13}	0.0	1.0
$\mathrm{HO_2} + \mathrm{HO_2} = \mathrm{H_2O_2} + \mathrm{O_2}$	1.0×10^{13}	0.0	1.0
$\mathrm{H_2O_2} + M$ $= \mathrm{OH} + \mathrm{OH} + \mathrm{M}$	1.2×10^{17}	0.0	45.5
$\mathrm{HO_2} + \mathrm{H_2} = \mathrm{H_2O_2} + \mathrm{H}$	7.3×10^{11}	0.0	18.7
$\mathrm{H_2O_2} + \mathrm{OH} = \mathrm{H_2O} + \mathrm{HO_2}$	1.0×10^{13}	0.0	1.8
$\mathrm{CO} + \mathrm{OH} = \mathrm{CO_2} + \mathrm{H}$	1.5×10^{7}	1.3	-0.8
$\mathrm{CO} + \mathrm{O_2} = \mathrm{CO_2} + \mathrm{O}$	3.1×10^{11}	0.0	37.6
$\mathrm{CO} + \mathrm{O} + M = \mathrm{CO_2} + M$	5.9×10^{15}	0.0	4.1
$\mathrm{CO} + \mathrm{HO_2} = \mathrm{CO_2} + \mathrm{OH}$	1.5×10^{14}	0.0	23.7
$\mathrm{OH} + M = \mathrm{O} + \mathrm{H} + M$	8.0×10^{19}	-1.0	103.7
$\mathrm{O_2} + M = \mathrm{O} + \mathrm{O} + M$	5.1×10^{15}	0.0	115.0
$\mathrm{H_2} + M = \mathrm{H} + \mathrm{H} + M$	2.2×10^{14}	0.0	96.0
$\mathrm{H_2O} + M = \mathrm{H} + \mathrm{OH} + M$	2.2×10^{16}	0.0	105.0

In the $H_2 - O_2 - CO$ mechanism, there are third-body (M) reactions of two species A and B to yield one single product species AB^*.

$$\mathrm{A} + \mathrm{B} = \mathrm{AB}^* \tag{2.14}$$

$$\mathrm{AB}^* = \mathrm{A} + \mathrm{B} \tag{2.15}$$

$$\mathrm{AB}^* + \mathrm{M} = \mathrm{AB} + \mathrm{M}^* \tag{2.16}$$

$$\mathrm{M} = \mathrm{M}^* + heat \tag{2.17}$$

The third body M is an inert molecule (in the atmosphere, generally N2 and O2) that can remove the excess energy from AB* and eventually dissipate it as heat [17].

The $H_2 - O_2 - CO$ mechanism will provide accurate values for flame characterization. Because the accuracy of the combustion simulations depends primarily on burned gas properties included in the system. In this regard, the more species/reaction will provide more accurate results. However, the computational time should not be skipped. The computational costs of a given reaction are proportional to N^2, where N is the number species. The acetylene-oxygen reaction with $H_2 - O_2 - CO$ mechanism includes 12 species (C_2H_2, O_2 , H, O,H_2,OH, H_2O,N_2, CO, CO_2, HO_2 and H_2O_2). Hence, the multi-step reaction model used in this study is computationally expensive than other reaction models explained earlier.

2.4 Reaction Models

2.4.1 Eddy-Dissipation Model

Magnussen and Hjertager have developed a concept for the mean reaction rate of species based on the turbulent mixing rate. This model supposes that most fuels are burning very fast, and the overall rate of reaction is completely dominated by turbulent mixing eddy. In such cases, it is possible to neglect the importance of chemical kinetic rates at the reaction region where can be defined with Damköhler numbers (Equation 2.18) greater than 1 [18].

$$Da = \frac{flow\ time\ scale}{chemical\ time\ scale} \tag{2.18}$$

In Ansys Fluent, the eddy-dissipation model can be created with more reactants and more products concept. This will ensure the flame to be simulated much better compared to the single-step global reaction. However, the model is only allowed to be used with the single-step reaction and without calculating the kinetics rate. This means every reaction has the same turbulent rate. That is why it is a likelihood to obtain incorrect results with the eddy-dissipation model due to Ansys Fluent restriction.

To remedy this, eddy-dissipation concept model which can predict kinetically controlled species and combine multi-step detailed chemical kinetic mechanisms in turbulent flows should be applied.

2.4.2 Eddy-Dissipation Concept Model

The eddy-dissipation-concept (EDC) model offered by Magnussen and Gran is an extension of the eddy-dissipation model. However, the idea is completely different. It assumes that reaction occurs in small turbulent structures and calculates a volume fraction of small scale eddies in which the reactions occur.

The EDC model can incorporate detailed chemical mechanisms into turbulent reacting flows. So It is more applicable than the eddy dissipation model for more complicated reaction mechanisms. However, complex reaction mechanisms are always stiff and numerical integrations to solve them is computationally expensive. Hence, the usage of the EDC model is recommended when the acceptance of fast chemistry is not valid such as in this study.

2.5 Conjugate Heat Transfer

The conjugate heat transfer is used to define processes which include the distribution of temperature inside the fluid zone and the solid zone, due to thermal contact. The thermal energy transition between bodies is described as the study of heat transfer. The heat always flows from hot region to cold one which is a direct consequence of the second law of thermodynamics [19]. It points out that this natural process happens only in one sense and can not be reversible.

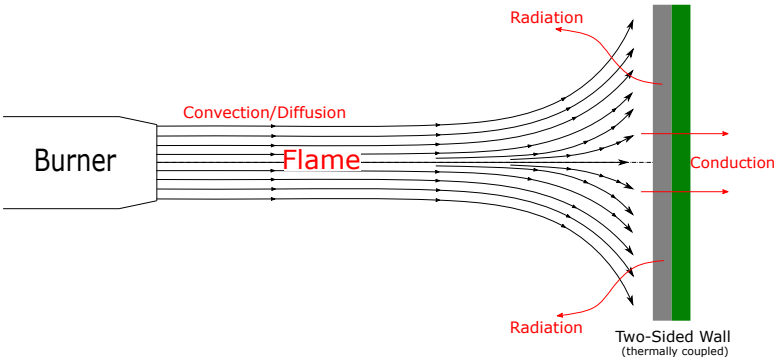

Figure 2.5: Simple illustration of the system with heat flux components

As an example of a simple illustration from this study (Figure 2.5), conjugate heat transfer can be formed with the combination of heat transfer components in solids and fluids. In solids, conduction often dominates whereas, in fluids, convection/diffusion usually dominates. The radiation in high temperatures has also importance as a component of heat flux from the solid to the ambient.

2.5.1 Heat Coupling at Interface

In the solution domain of the current system(Figure 2.5), there are two physically different cell zones, called fluid and solid zone. In these cases, two-sided wall pairs should be generated to create thermal relation between different cell zones. In this regard, Ansys Fluent will automatically create wall-wall shadow pairs after creating a mesh with this type of zones.

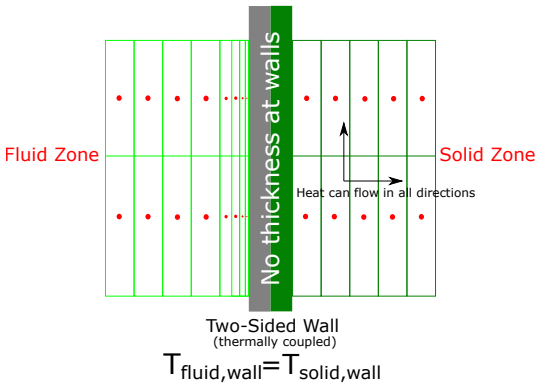

Figure 2.6: Two-Sided walls

In the simulation setup section, different thermal conditions such as heat flux and temperature can be defined separately to these two-sided walls. However, specifying different thermal conditions on each wall will create two different and separate walls which are perfectly insulated from each other. Therefore, the walls should be considered as a coupled boundary condition. In this type of boundary condition, the walls will be thermally coupled without defining additional thermal boundary condition. The solver will calculate heat transfer directly from the material properties and the solution in the adjacent cells.

The heat transfer as mentioned before happens in three ways. The convection which is due to the macroscopic motion of the mass in the domain, in fact, directly depends on the velocity field (second term on the left-hand side of the energy equation Equation 2.3). There are different ways for the generation of convection. Free, or in other words natural, convection appears when bulk fluid motions are affected by buoyancy forces that result from density variations due to variations of temperature in the fluid [20]. Another formation of convective heat transfer is called forced convection. In this process, the fluid is directly forced by a pump, fan or other mechanical tools [20]. The convective heat transfer also includes the heat movements by diffusion. Diffusion happens at a molecular level and can be expressed with the Fourier law (first term on the right-hand side of the energy equation Equation 2.3) [20]. The conduction is a particular case of diffusive heat fluxes that happens in rigid solids, but this is definitely called heat conduction.

The thermo-fluid dynamic quantities and therefore the chemical compositions within the fluid domain close to the solid material, and then the convective heat flux, are affected by the temperature fields exists on the material surface. So, a correct approach, the one considering the interaction between the fluid (f) and the solid material (s), should be established taking into account temperature and heat flux continuities:

$$T_{f,wall} = T_{s,wall} \tag{2.19}$$

$$k_f \frac{\partial T}{\partial n}\bigg|_{f,wall} + \dot{q}_{chem} = k_s \frac{\partial T}{\partial n}\bigg|_{s,wall} + \dot{q}_{rad,out} \tag{2.20}$$

where n is the normal direction of the interface. In the equation, $\dot{q}_{chem}$ is the chemical contribution to the heat transfer (due to the dissociation/recombination reactions occurring at the solid/fluid interface) and $\dot{q}_{rad,out}$ is the radiative heat flux emitted by the solid surface.

2.5.2 Radiation

On the contrary to heat conduction, thermal radiation does not require a physical mean to transmit its energy. Rather, it is transported at the speed of light via electromagnetic waves [20]. However, from the broad electromagnetic spectrum, only the part that can be perceived as light or heat is named as thermal radiation. This corresponds to a bandwidth of approximately 0.4 μm to 1 mm, which covers visible light and the infrared radiation.

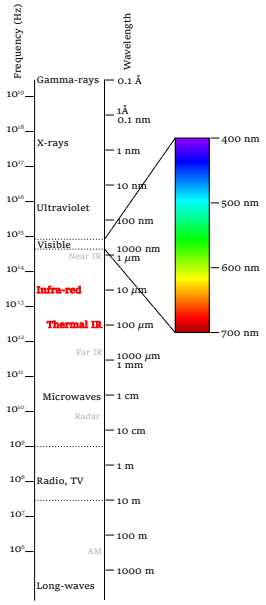

Figure 2.7: The electromagnetic spectrum [21]

Entire bodies in-universe can radiate energy in the formation of photons in any direction with arbitrary phase and frequency. These radiated photons might be absorbed, transmitted and/or reflected. This process can be illustrated by following Figure 2.8 [22]:

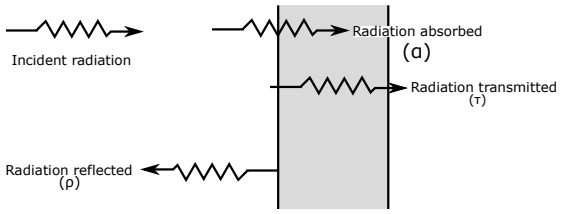

Figure 2.8: Radiation surface properties

where

- α is the absorptance
- ρ is the reflectance
- τ is the transmittance

If thermal radiation has coincided with the material, energy is transferred into it depending on the degree of absorption. The principle of energy conservation, which means that the sum of absorbed, reflected and transmitted radiation must be equal to the amount of incident energy, is valid here. The relationship between the degree of absorption α, the degree of reflection ρ and the degree of transmittance τ is shown in Equation (2.21) [22][23].

$$\alpha + \rho + \tau = 1 \tag{2.21}$$

For example, if one term of this equation disappears, the term black body arises. This is the ideal image of a body whose degree of absorption is equal to 1, which means that all of the incident heat radiation is absorbed. Due to the radiation balance, absorbed energy must also be released again. Hence, the energy radiated is established according to Stefan-Boltzmann law [23].

$$P = (\frac{E}{E_b})\sigma T^4 = \varepsilon \sigma T^4 \tag{2.22}$$

where E is radiation from the real body at T, and E_b is radiation from a black body at T. In case having black body, ε, emissivity, is equal to 1.

As it is mentioned in section 2.2, radiation heat transfer should be considered with a separate transport equation which is well-known as Radiative Transfer Equation(RTE) [13][23]. The RTE for an absorbing, emitting, and scattering medium at position $\vec{r}$ in the direction $\vec{s}$ is

$$\frac{\partial I}{\partial x_i} + \underbrace{(a+\sigma_s)\, I(\vec{r},\vec{s})}_{Absorption} = \underbrace{an^2 \frac{\sigma T^4}{\pi}}_{Emission} + \underbrace{\frac{\sigma_s}{4\pi} \int_0^{4\pi} I\left(\vec{r},\vec{s}'\right) \Phi\left(\vec{s}\cdot\vec{s}'\right) d\Omega'}_{Scattering} \tag{2.23}$$

where

- $\vec{s}'$ is scattering direction vector
- α is absorption coefficient
- n is refractive index
- σ_s is scattering coefficient
- σ is Stefan-Boltzmann constant
- I is radiation intensity,which depends on position vector and direction vector
- Φ is phase function
- Ω' is solid angle

This equation should be included in the simulations when the radiative heat flux is larger than convective or conductive heat flux. Being larger also means that the fourth-order dependence of the radiative heat flux (Equation 2.22) shows the domination of the radiation in the system. The first term on the left-hand side represents the rate of change by the radiation intensity. This term allows radiation intensity to change from cell to cell as it is like in reality. Otherwise, it is more likely to have the same in every cell in the solution domain. The first term on the right-hand side is an emission that emits the radiation proportional to the fourth power of the temperature. Finally, to understand the last term on the right-hand side, the radiation model should be considered firstly. Because this term directly depends on the number of directions to be solved by radiation models.

There are five radiation models to solve the radiation transfer equation [13]. In this study, the discrete ordinates (DO) radiation model will be utilized. The DO model can account for gaseous participation which means that the gas absorbs and scatters the radiation. As an example of participation to radiation, CO_2, H_2O and soot can participate in radiation whereas H_2, N_2 and O_2 do not participate. The general advantage of the DO model is being comprehensive compared to other methods. This method accounts for scattering, semi-transparent media, specular surfaces, and wavelength-dependent transmission using the banded-grey option. Besides, it enables users to solve surface-to-surface radiation in combustion problems if necessary.

The DO model discretizes the beam direction ($\vec{s}$) to minimum 4 directions in 2D and 8 directions in 3D. In this study, the 2D model is being considered. Hence, the integral over all directions becomes a summation of these 4 directions.

The scattering summation provides the ability to transfer energy between the direction. In the end, one source term will appear for every other beam directions that collect all into the current direction. As it is understood, the CFD studies which have radiation inside, have an extra 4 equations (2D) to be solved. This is cumbersome in the sense of computational time. Therefore, it is highly recommended to solve the radiation equations for every 10 iterations of the energy equation instead of every 1.

Chapter 3

Experimental Setup and Numerical Domain

3.1 Experimental Facility

The experimental facility can be seen in Figure 3.1. The system consists of linear axes driven by to stepper motors automatically. This enables the precise movement of the materials into flame.

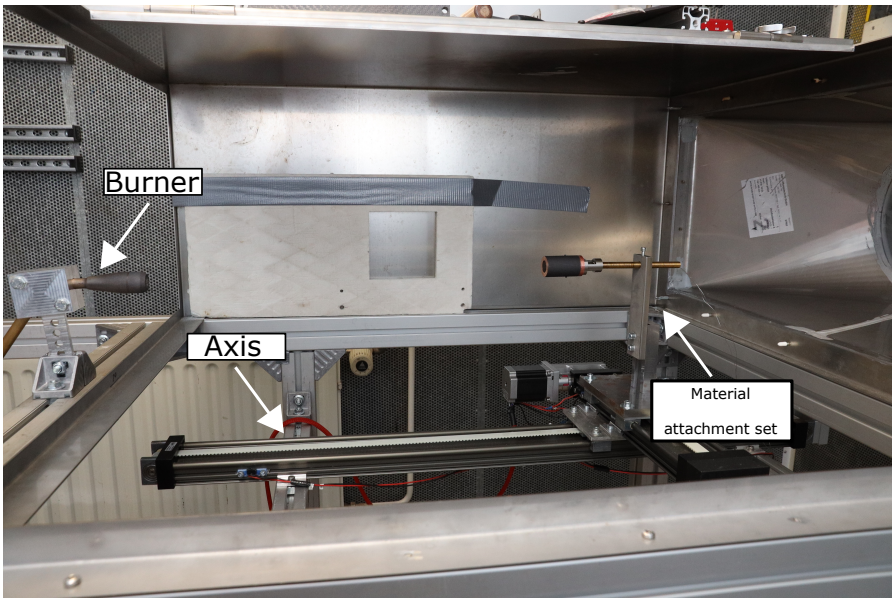

Figure 3.1: The experimental setup

The driven motors are controlled employing TMCM-3110-TMCL driver board of Trinamic Motion Control GmbH and Laboratory Virtual Instrumentation Engineering Workbench (LabVIEW). An i100 instruNet records the temperatures. Besides, two Bronkhorst mass flow controllers which enable precise setting and control of the gas mixture ratio are installed.

3.2 Numerical Domain

The numerical domain is one of the most important parameters in most CFD calculations. It should be considered by taking into account the discretization of the optimum possible area to reduce the computational effort and the influence of the approximations of the boundary conditions.

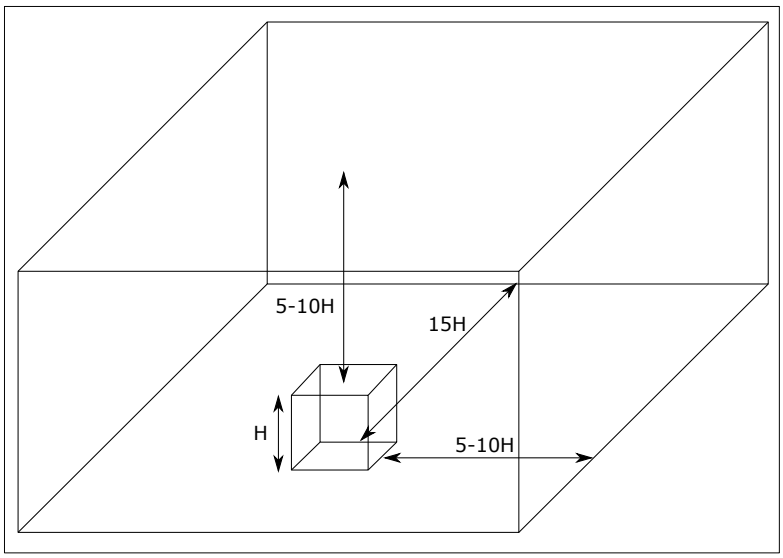

Figure 3.2: The minimum domain limits for CFD simulations

The Figure 3.2 shows the domain limitations emphasized in the article about the recommendations of the COST: Best Practice Guideline for the CFD [24]. However, these limits are the minimum so in our case, the upper limit which is more important in this study will be considered as $15H$ where H is $0.015m$.

The numerical domain consists of one acetylene-oxygen burner inlets and tested materials with one holder, insulator material and the sample material used for heat shields in spacecraft. The burner inlets and the material zone will be well explained in the following

chapters. 2-dimensional axisymmetric domain assumption will be considered in the simulation procedure since the 3-dimensional domain of the concerned problem is computationally expensive to conduct successive simulations concerning changing parameters such as different materials variations.

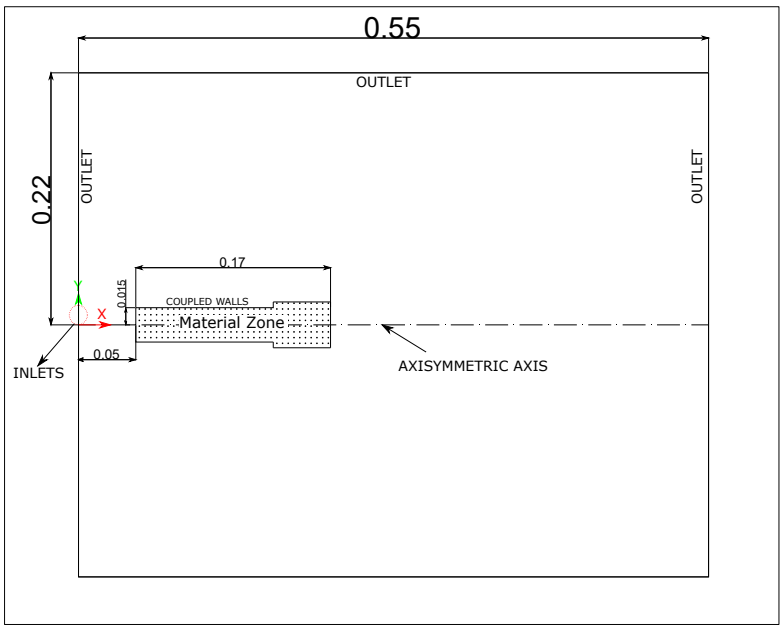

Figure 3.3: The numerical domain and boundary conditions

In Figure 3.3, the dimensions are in terms of meter. The materials are placed at a distance of $50mm$ from the burner inlets. The experimental facility is nor enclosed volume. So, the entire volume will be modelled with an outlet boundary to provide atmospheric conditions. The coupled wall boundary conditions will be evaluated when the material zone in the conjugate heat transfer is activated. The lower half of the domain is not being considered while generating simulations. The point to be considered here is that the rotation axis should be designed as the x-axis.

Chapter 4

Numerical Simulation

ANSYS Fluent (Fluent Inc., Lebanon, New Hampshire, USA) is a very powerful and flexible CFD software. The capabilities of the software enable studies on several types of fluid-dynamic problems: compressible and incompressible, steady and unsteady, two-dimensional (2D) and three-dimensional (3D) flow. The software allows also the study of turbulence phenomena and of reaction kinetics. These last capabilities are usefully exploited in the particular presented application, which involves the study of the mixing and combustion between oxidant and fuel and the heat generation and transfer between gas and solid phases. ANSYS Fluent is preferred in this study due to fulfilling all necessities for the solution of the considered problem.

4.1 Simulation Procedure

The simulation procedure conceptually consists of 3 major steps that depend on each other firmly. These are cold flow, combustion and conjugate heat transfer respectively. These steps being interconnected intend that each will form an initial condition for the next step. This step by step solution method ensures the computationally stiff system to work in a stable manner when the additional transport equations and/or species and reactions are added into the solution domain to be solved. The simulation procedure can be expressed in Figure 4.1

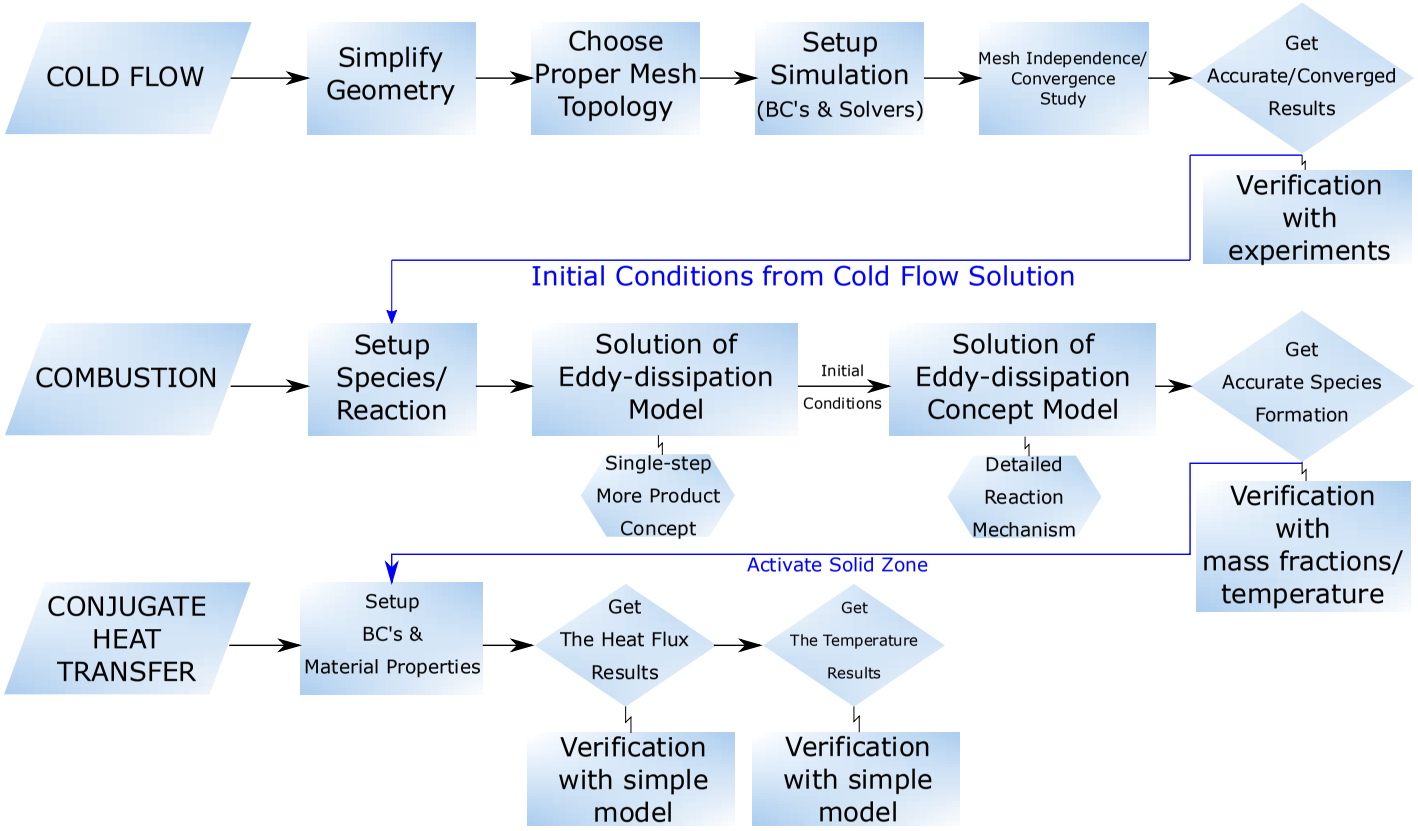

Figure 4.1: The simulation procedure

As it is explained before, one of the most important parameter for CFD application is the mesh independence and convergence study. Both of them will be performed in the first step of the simulation called Cold Flow (or without reaction) requiring less computational power. At the same time, the cold flow will produce good initial conditions consisting of the basic flow patterns. In this step, the simulation will be carried out with the flow, turbulent, energy and species equations with reaction disabled. To be able to understand whether the system has been established with a proper mesh topology/structure, the pressure quantity at the middle of the sample material taken from experiment and obtained from CFD calculation will be examined. Afterwards, the reactions will be activated and will be solved with eddy-dissipation and eddy-dissipation concept model respectively. To judge whether the flame has been characterized accurately, either the concentration of oxygen, acetylene inside the flame or the maximum temperature of the flame can be investigated. Both of them will be used as a verification method in this study. In the last step regarded as the conjugate heat transfer, the solid zone will be activated and then considering fluid-solid zone interactions, the boundary conditions and the material properties will be implemented meticulously. The evaluations at the last step will be processed in terms of the overall heat flux acting on the material and corresponding temperature distribution. Consequently, the whole system will be tried out with different material combinations.

4.2 Cold Flow

4.2.1 The Burner Head Simplification

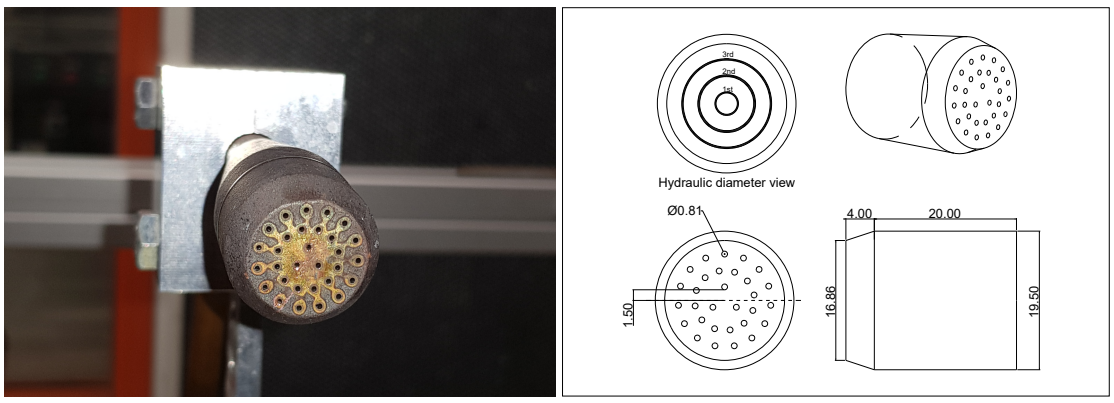

(a) (b)

Figure 4.2: The acetylene-oxygen burner head; (a) the view taken from the experimental facility; (b) the technical drawings

As seen in the Figure 4.2, there are acetylene-oxygen mixture inlet holes in 3 different axes in the burner head. When turning the burner head into the 2D axisymmetric domain, the hydraulic mean diameter must be calculated to maintain the momentum conservation. In this calculation, the area of each hole is calculated and then, the hydraulic diameter is determined as seen in Table 4.1 so that the total wet area remains constant.

Table 4.1: The hydraulic diameters at the inlet

Annular holes	Hydraulic diameter (mm)
1st (inner) hole	0.1559
2nd (inter) hole	0.2500
3rd (outer) hole	0.1978

4.2.2 The Mesh Generation

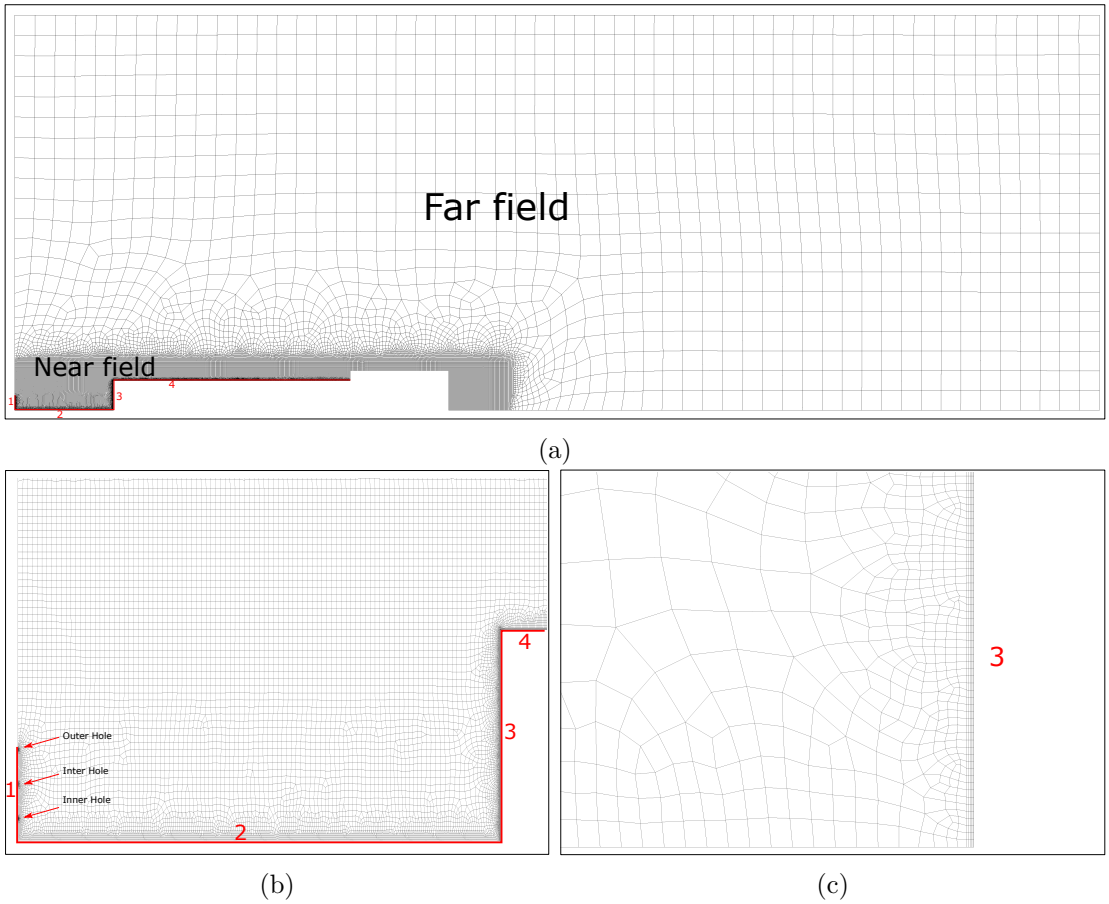

Figure 4.3: The mesh topology; (a) the general view of the fluid mesh zone; (b) the edge refinement regions; (c) the view of near-wall treatment at the 3rd edge

The mesh employed in this study is unstructured quad-dominant with triangle elements in the smoothing regions. As seen in Figure 4.3, the solution domain is divided into two parts for spatial discretization. These are the near-field and the far-field.

As it is a known fact that the important flow phenomena will occur around the geometry. Therefore, the near-field region must be created to cover all geometry from the burner head where is the exit region of the flame. The reason for the generation of the mesh at the near-field from the burner head is that the sudden mesh size changes in the flow direction may cause instability in the equations, which may lead to non-converged results. So, the near-field should be performed to capture the entire structure of the flame more finely. To achieve a smooth transition between fine and coarse mesh regions, the smoothing algorithm is used. Besides, more efficient modelling of the turbulence zone that increases as it moves away from the flame centre is provided in this smooth transition zone where is between the near-field and far-field.

As shown in Figure 4.3, the edge refinements have also been made. The properties of edge refinements can be seen in Table 4.2.

Table 4.2: The edge refinements properties

	Number of elements (-)	Element size (mm)
1st (inner) hole	10	0.015
2nd (inter) hole	10	0.025
3rd (outer) hole	10	0.019
2nd line	500	0.1
3rd line	450	0.03
4th line	1000	0.12
Inflation layer at 3rd/4th line	5	-

The mesh sizes are refined at the inlet holes. Thus, it is aimed to obtain high resolution in the first region where the combustion will take place. The high gradients near walls will be better covered by performing near-wall treatments along the third and fourth edge lines. The second edge line is the axisymmetric axis. There are two reasons for applying edge refinement at this line. Firstly, the high turbulence zone is expected at the core of the burner head and secondly, the simulations are mainly performed to see the results which are at the mid of geometry. Therefore, it is aimed to model this zone finer by refining the line.

4.2.3 Pre-processing

4.2.3.1 Boundary Conditions

The inlet conditions:
The acetylene-oxygen mass ratio should be obtained by taking into account the reaction equation.

$$\omega_{O_2} = \frac{m_{O_2}}{m_{O_2} + m_{C_2H_2}} = \frac{159.994g}{159.994g + 52.075g} = 0.75 \tag{4.1}$$

To provide stoichiometric mixture condition which is also named as a balanced chemical equation, the ratio calculated in Equation 4.1 should be utilized. The stoichiometric mixture ratio means that exactly enough air is provided to completely burn all of the fuel. Hence, the flame will be neither rich nor lean but exactly balanced. All simulations and experiments will be conducted under the stoichiometric condition. The acetylene-oxygen mixture will be injected into the system through 3 different hydraulic diameters even if combustion has not been activated yet. So, the total mass flow should be divided proportionally concerning wet areas.

Table 4.3: The inlet boundary conditions

	Acetylene	Oxygen	Total Mass Flow (g/s)
Mass flow inlet (g/s)	0.292	0.898	1.19
Species Mass Fraction	0.25	0.75	
	1st (inner) hole	2nd (inter) hole	3rd (outer) hole
Mass flow inlet (g/s)	0.1188	0.4752	0.594
Turbulent intensity (%)	5	5	5
Turbulent viscosity ratio	10	10	10
Temperature (K)	300	300	300

Finally, turbulent properties have been taken as default values offered by Ansys Fluent since these parameters should be normally obtained experimentally. However, Ansys Fluent default turbulent parameters will provide a good initial start for problem solution.

The walls and outlet conditions:
As it is known, the air contains mostly nitrogen (78.09%) and oxygen (20.95%). Thus, nitrogen and oxygen are defined as 0.8 and 0.2, respectively, to create atmospheric conditions at outlet boundary conditions. On the other side, the walls should be created as no-slip boundary conditions since the velocity gradients should be zero at the walls. Besides, the

zero-gradient (zero-flux) boundary condition for all species should be also considered because there is no reaction happening at the walls.

Table 4.4: The walls and outlet boundary conditions

OUTLET				**WALL**	
	Acetylene	Oxygen	Nitrogen		
Species Mass Fraction	0	0.2	0.8	Momentum	No-slip stationary wall
Turbulent intensity (%)		5		Thermal Boundary Conditions	-
Turbulent viscosity ratio		10		Species Boundary Conditions	Zero diffusive flux
Temperature (K)		300		Wall Roughness	Standart

4.2.3.2 Solver

The model is axisymmetric, and this reduces the computational cost. In addition to the classic Navier–Stokes equations for mass, momentum, and energy conservation, the flow is modelled assuming: (i) an ideal gas behaviour, (ii) turbulence model. The turbulence model has been selected as k-omega SST. The solver properties and solver controls, in other words, relaxation factors, can be seen in the Table 4.5.

Table 4.5: The solver properties for cold flow simulations

Solver Algorithm	Coupled	
	Spatial Discretization	**Relaxation Factors**
Gradient	Least squares cell based	-
Pressure	Linear&second order	0.5
Density	First order upwind	0.25
Momentum	First&second order upwind	0.5
Energy	First order upwind	0.75
Turbulent Properties	First&second order upwind	0.75

The first-order and the second-order upwind schemes will be applied for some equations respectively. Firstly, the simulations will be run with the first-order upwind scheme and afterwards, the solutions obtained from first-order schemes will be used as an initial guess for the second-order upwind schemes.

As it is mentioned in simulation procedure solving reacting flow with two-step solution process will ensure a stable converged simulation. In this regard, the procedure for the cold flow simulations should be done as below:

- Set up all species and reactions of interest

- Disable the reaction calculations by turning off *"volumetric"* in the species model dialogue box
- Turn off the species equations to be solved
- Finally, calculate a cold flow (initial) solutions

These settings allow reproducing and simulating the cold flow with a high degree of accuracy, correlating the process not only to the fluid-dynamic field but also to turbulence. Thus, it will be providing good initial conditions for combustion processes.

4.2.4 Mesh Independence and Convergence Study

The more accurate settings done so far, the more accurate converged solution will be. However, the last things that needed to be done are convergence and mesh independence study. The convergence study might be carried out in two senses:

- RMS residual errors should be reduced to an acceptable value (nearly 10^{-4} or 10^{-5})
- Monitor probe for values of interest should be reached a steady solution.

Although the simulations have converged based on residual levels and monitor probe, the mesh independence study should be carried out simultaneously to be sure that the solution is also independent of the mesh resolution. Hence, the different mesh cell size should be created and followingly, it should be checked whether there is any change with the mesh size.

Table 4.6: The mesh properties of different mesh types

	The Mesh Sizes		**The Element Types**		**The Mesh Qualities**		
	Near-field (mm)	Far-field (mm)	Quad Elements	Triangle Elements	Orthogonality	Aspect Ratio	Skewness
Coarse Mesh	1	10	27087	612	0.95	2.55	0.15
Fine Mesh	0.5	10	38086	657	0.97	2.27	0.13
Finer Mesh	0.325	10	58491	695	0.97	1.99	0.10

The different meshes, 1.5 times of each other, has been generated. The simulations are carried out for each mesh types and the convergence is tested with the probe which is placed at the mid of the geometry and with the final residuals.

Table 4.7: The final residuals of different mesh sizes

	The Final Residual					
	Continuity	X-velocity	Y-velocity	Energy	k	omega
Coarse Mesh	$1.5280{\cdot}10^{-5}$	$4.3094{\cdot}10^{-8}$	$4.4495{\cdot}10^{-8}$	$5.9658{\cdot}10^{-11}$	$7.3715{\cdot}10^{-9}$	$4.8004{\cdot}10^{-7}$
Fine Mesh	$6.2084{\cdot}10^{-6}$	$3.1504{\cdot}10^{-8}$	$3.1473{\cdot}10^{-8}$	$1.4721{\cdot}10^{-11}$	$5.5097{\cdot}10^{-9}$	$4.4938{\cdot}10^{-7}$
Finer Mesh	$9.4392{\cdot}10^{-6}$	$4.2856{\cdot}10^{-8}$	$4.4168{\cdot}10^{-8}$	$8.4518{\cdot}10^{-11}$	$7.3486{\cdot}10^{-9}$	$4.7995{\cdot}10^{-7}$

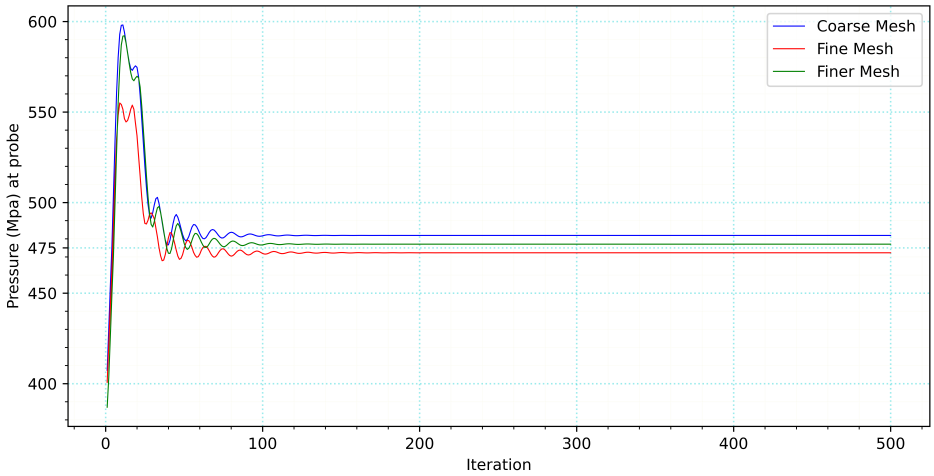

Figure 4.4: The convergence behaviour of the pressure variable at the probe

The results are independent of the mesh sizes by taking into account the Figure 4.4. Each mesh sizes give nearly the same result. The residual levels are met with universal criteria. However, the fine mesh will provide good enough resolution for the next simulations. As the distance from burner head changes, convergence and mesh independence study should be carried out separately. However, the sample material is placed at 50mm for all material variations. Hence, the same mesh topology and mesh refinements will be used for all simulations.

4.2.5 Results

Figure 4.5 shows the velocity profile of the cold flow. The maximum velocity occurs in the inlet (in zone A). Turbulence or vortex field in zone D indicated in Figure 4.5(b) is quite intense as expected. In these regions, the speed falls below the average.

The velocity profile beyond the high turbulent region at the inlet can be generally expressed by the zone C on the scale.

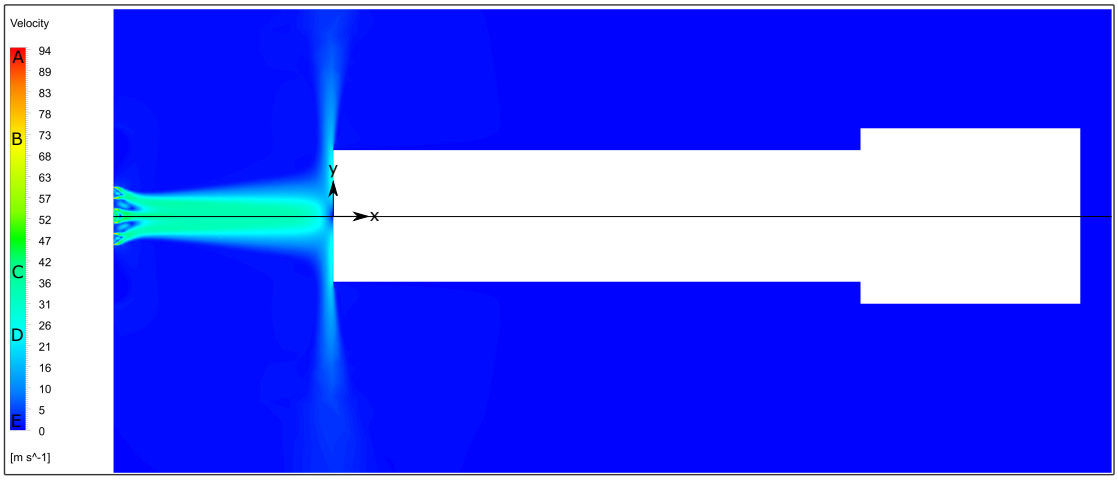

(a)

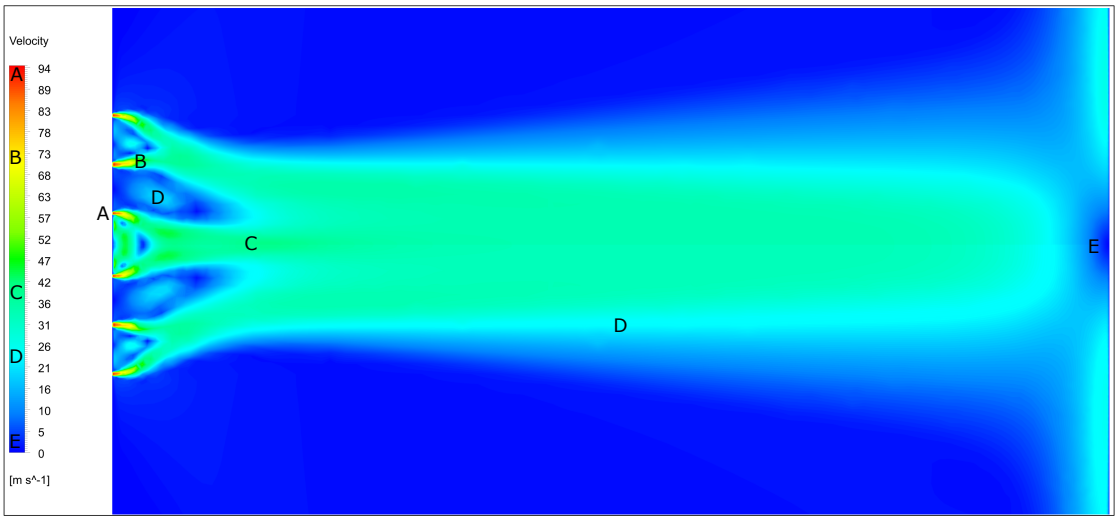

(b)

Figure 4.5: The velocity distribution of the cold flow simulation

On the front surface of the geometry, the stagnation point occurs in the middle of the geometry. In this region, the velocity is zero and pressure is in its maximum. As can be seen in Figure 4.6, the maximum pressure occurred in the middle point and the pressure drop is observed with the increase in the velocity along the front surface.

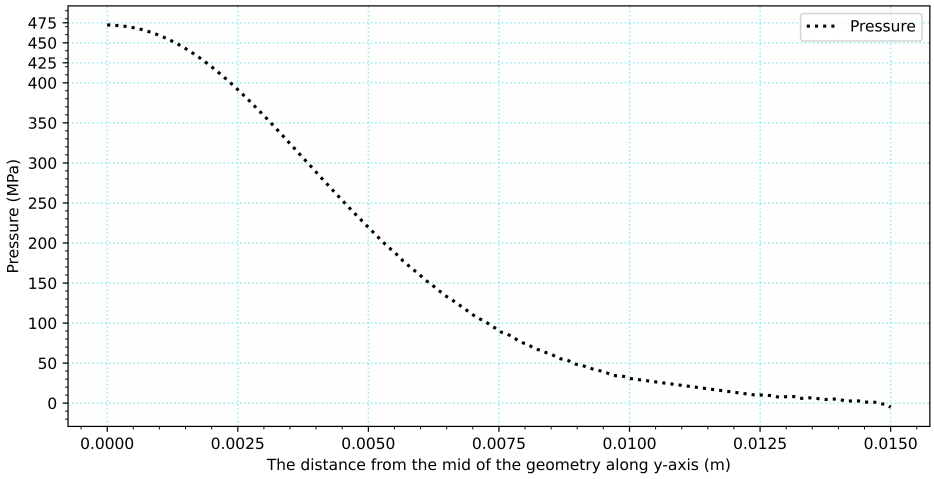

Figure 4.6: The pressure distribution of the cold flow over the front surface

Table 4.8 shows the comparison between numerical simulations and experimental measurements [25]. In the experiment, the pressure probe has been placed in the middle of the geometry. The variation shows that the numerical simulation is perfectly matched experimental result with a very good agreement.

Table 4.8: The per cent variation between numerical simulation and experimental measurements of pressure quantity

Quantity	Numerical Simulation	Experimental Measurement	Variation (%)
Pressure at stagnation point (MPa)	472.22	470	0.47

All in all, the velocity profiles and the pressure distribution over the front surface of the geometry proves that the cold flow is modelled with a high degree of accuracy. Hence, the basic flow patterns obtained from cold flow simulations will provide good initial conditions for the next step called combustion.

4.3 Combustion

The acetylene is an extremely flammable gas produces a high-temperature flame over 3,300 K, in case of interaction with oxygen. It is very well-known that oxyacetylene combustion happens very fast [26]. As seen in Figure 4.7, the whitish-blue flame at the core is much smaller than the blue flame due to access of the oxygen. The specimen probe was also placed at a distance of 50 mm.

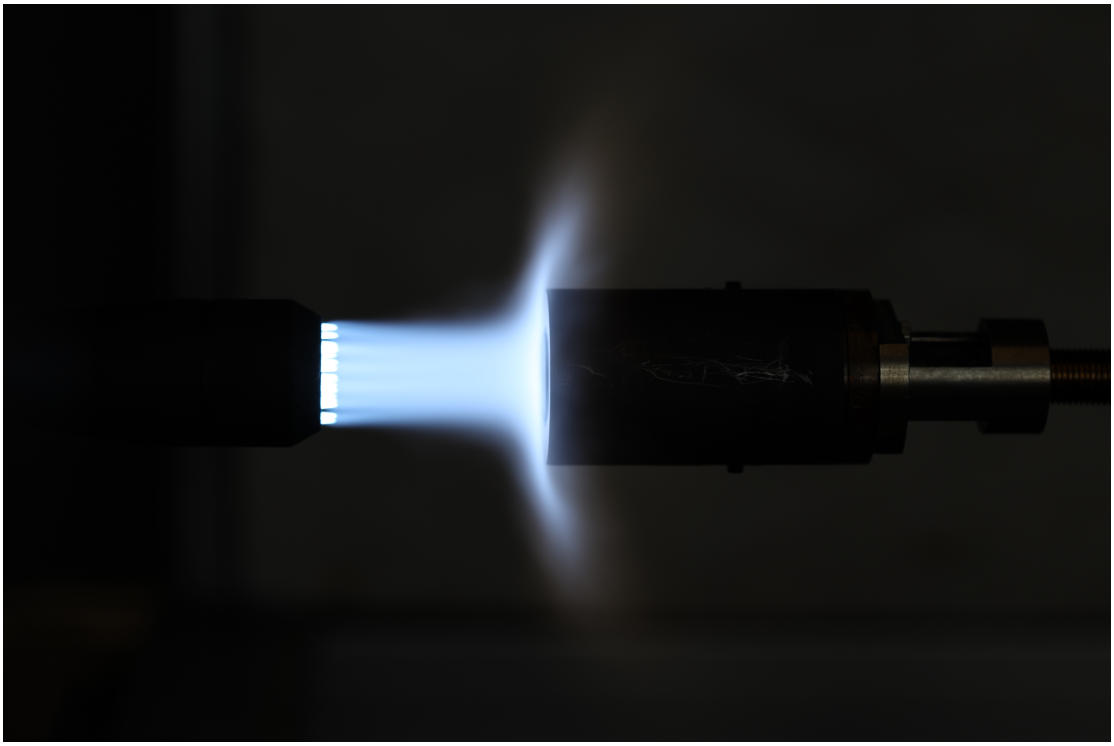

Figure 4.7: The oxyacetylene flame when the heat flux probe is at a distance of 50 mm

4.3.1 Eddy Dissipation Model

4.3.1.1 Pre-processing

The single-step more product reaction concept given earlier will be utilized in the eddy dissipation model. The main reason for using this concept with the eddy dissipation model is that the detailed reaction mechanisms with extended reaction rates, can not be implemented to Ansys Fluent together with eddy dissipation model. This is a limitation of this model.

Table 4.9: Acetylene-oxygen mixture properties for eddy-dissipation model

Property	**Assumtion**
Reaction	Eddy-dissipation
Density (kg/m^3)	Incompressible ideal gas
Specific Heat (Cp) (j/kgK)	Mixing law
Thermal Conductivity (w/mK)	0.0454
Viscosity (kg/m-s)	1.72e-05
Mass Diffusivity (m$^2/s$)	2.88e-05

The flow properties can be seen in Table 4.9. Some of the flow properties are accepted as constant suggested by Ansys Fluent rather than ideal gas assumptions. Because this will reduce the computational time and will provide good initial flame structure for the eddy dissipation concept model.

Table 4.10: The solver properties for eddy-dissipation model

Solver Algorithm	Coupled	
	Spatial Discretization	**Relaxation Factors**
Gradient	Least squares cell based	-
Pressure	Second order	0.5
Momentum	Second order upwind	0.5
Energy	Second order upwind	0.75
Species	Second order upwind	0.75
Turbulent Properties	Second order upwind	0.75
Body Forces	-	1

The whole system includes 10 species which are solved simultaneously. As it is mentioned in the theory part, the computational cost will increase proportionally to N^2 where N is the number of species. This will make the system computationally very stiff. Therefore, the relaxation factor for species should be defined to stabilise the equations and correspondingly to get converged results. The given relaxation factors will provide a stable and converged solution.

4.3.1.2 Results

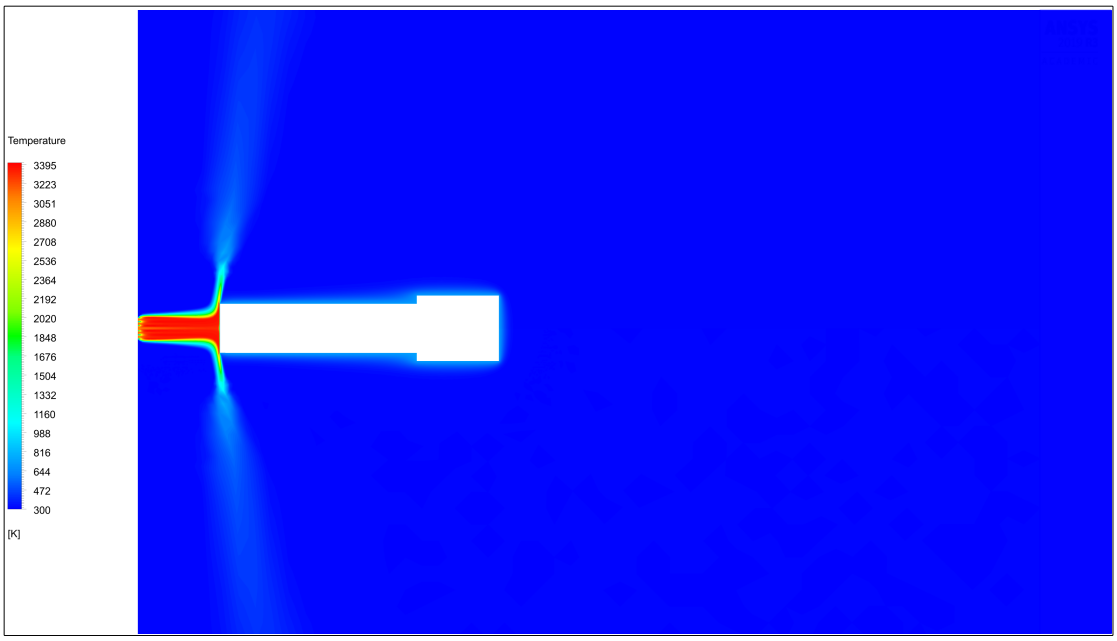

(a)

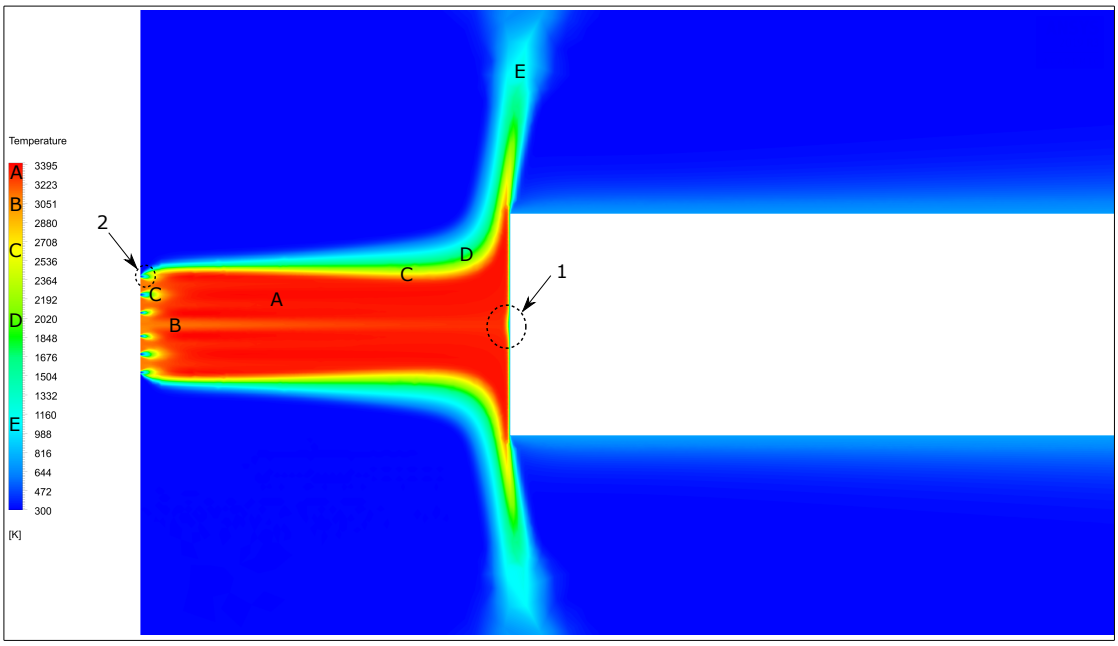

(b)

Figure 4.8: The temperature distribution of eddy dissipation model

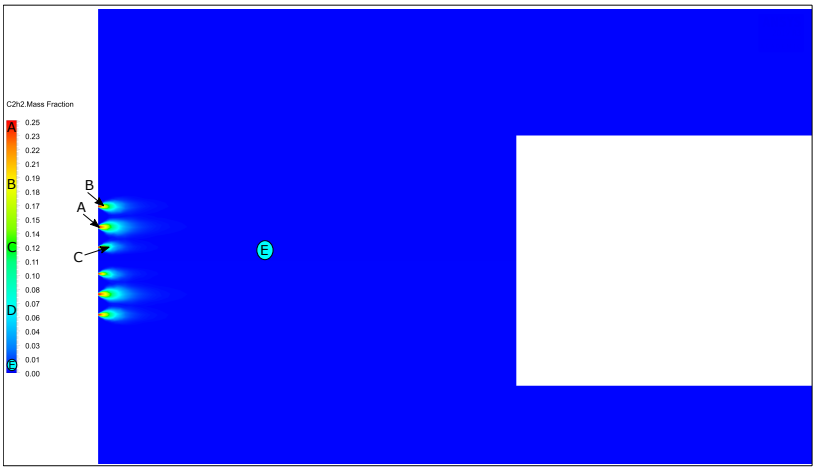

(a) Acetylene mass fraction

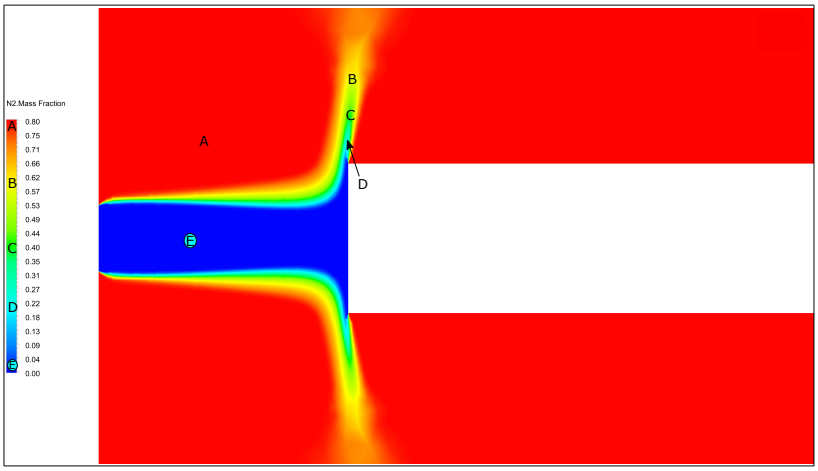

(b) Nitrogen mass fraction

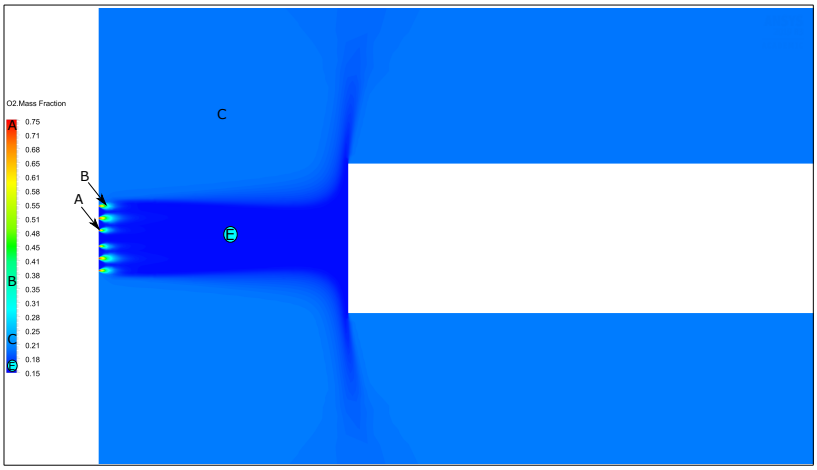

(c) Oxygen mass fraction

Figure 4.9: The mass factions of species in eddy dissipation model

The Figure 4.8a shows the temperature fields of numerical solution of eddy-dissipation model. The maximum temperature reaches up to 3395 K at the flame centre as expected. However, it is clear in the Figure 4.8b that there are few problems in the flame structure direct consequence of using inadequate chemical reaction mechanism and flow properties. The non-physical temperature decrease exists in the flame centre depicted with zone B. Furthermore, the first dashed circle ring near the sample material has another non-physical low-temperature field. Finally, the second dashed ring at the third inlet hole shows nonuniform temperature field which is indicative of weak burning process.

The physical reasons for the inaccuracy of the eddy-dissipation model in the estimation of the temperature field can be partly found in the way the reaction 2.12 has been defined. The stoichiometric coefficient of the products has been determined based on the equilibrium composition in stoichiometric conditions. For example, the Figure 4.9c shows that the minimum oxygen mass fraction in the domain is around 0.15 as same as the mass fraction in case of stoichiometric condition which is determined by NASA Chemical Equilibrium Application in the appendix, Figure A.3. Although this is one of the best ways to use this approach (which is also widely used in the literature), it should be taken into account that in the real case the local conditions are not always stoichiometric. Consequently, the local chemical composition is not accurately computed, propending for an overestimation of the concentration of radicals and intermediate species, and a consequent underestimation of the flame temperature.

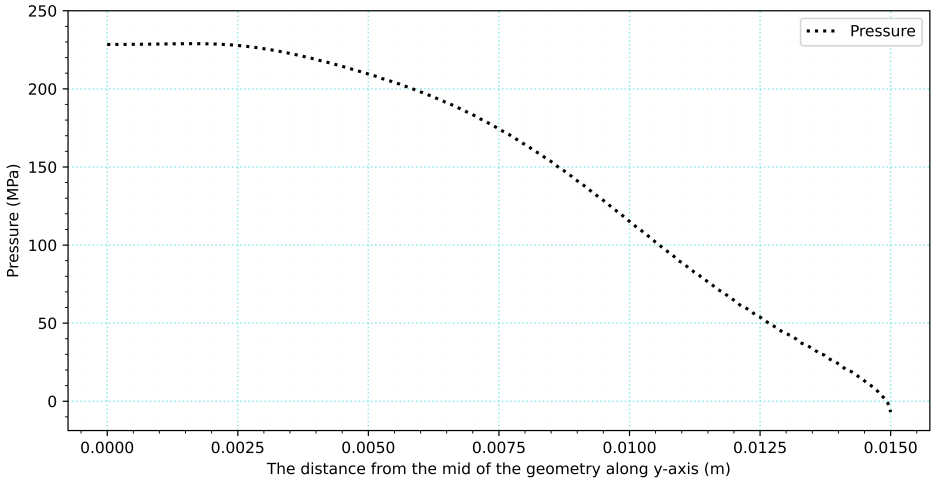

Figure 4.10: The pressure distribution of eddy dissipation model over the front surface

The Figure 4.10 represents pressure distribution which is estimated numerically over the front surface. The maximum pressure occurs at the mid of the sample material. The variation in Table 4.11 shows that numerical and experimental result at the probe, placed at the mid of the material, are close to each other with a good agreement. This also proves that the eddy dissipation model generates good initial flow pattern for further improvement.

Table 4.11: The per cent variation between numerical simulation and experimental measurements of pressure quantity for the eddy dissipation model

Quantity	Numerical Simulation	Experimental Measurement	Variation (%)
Pressure at stagnation point (MPa)	228.41	240	4.82

4.3.2 Eddy Dissipation Concept Model

4.3.2.1 Pre-processing

The multi-step detailed reaction mechanism will be used in the eddy dissipation concept model. This will remove the drawbacks of the eddy dissipation model and generate a more accurate solution.

Table 4.12: Acetylene-oxygen mixture properties for the eddy dissipation concept model

Property	**Assumtion**
Reaction	Finite rate
Density (kg/m^3)	Ideal gas
Specific Heat(Cp) (j/kg-K)	Mixing law
Thermal Conductivity (w/m-K)	Ideal gas mixing law
Viscosity (kg/m-s)	Ideal gas mixing law
Mass Diffusivity (m^2/s)	Kinetic theory

The flow properties are given in the Table 4.12. As it is well known that many species such as oxygen, nitrogen and carbon dioxide and most gases at high temperatures behave like an ideal gas. Therefore, the second further improvement in the oxyacetylene flame is the assumption of the compressible ideal gas. The last assumption is the kinetic theory. The kinetic theory explains the transport properties of the particles such as mass diffusivity. The thermal conductivity and viscosity of all species, apart from oxyacetylene mixture properties,

should be modelled with kinetic theory. In this way, the kinetic energy transfer which is strictly thermal due to particular interactions such as collisions will be better modelled.

Table 4.13: The solver properties for eddy-dissipation model

Solver Algorithm	Coupled	
	Spatial Discretization	**Relaxation Factors**
Gradient	Least squares cell based	-
Pressure	First order	0.5
Momentum	First order upwind	0.5
Density	First order upwind	0.25
Energy	First order upwind	0.5
Species	First order upwind	0.5
Turbulent Properties	First order upwind	0.75
Body Forces	-	1

The system involves 12 species, 22 reactions and 6 flow transport equations. Therefore, the whole equations are considered with first-order upwind schemes to reduce computational time and to increase stability. The relaxation factors for species and energy transport equations should be reduced to 0.5. The relaxation factor of the density which is determined as 0.25 provides a more stable solution.

4.3.2.2 Results

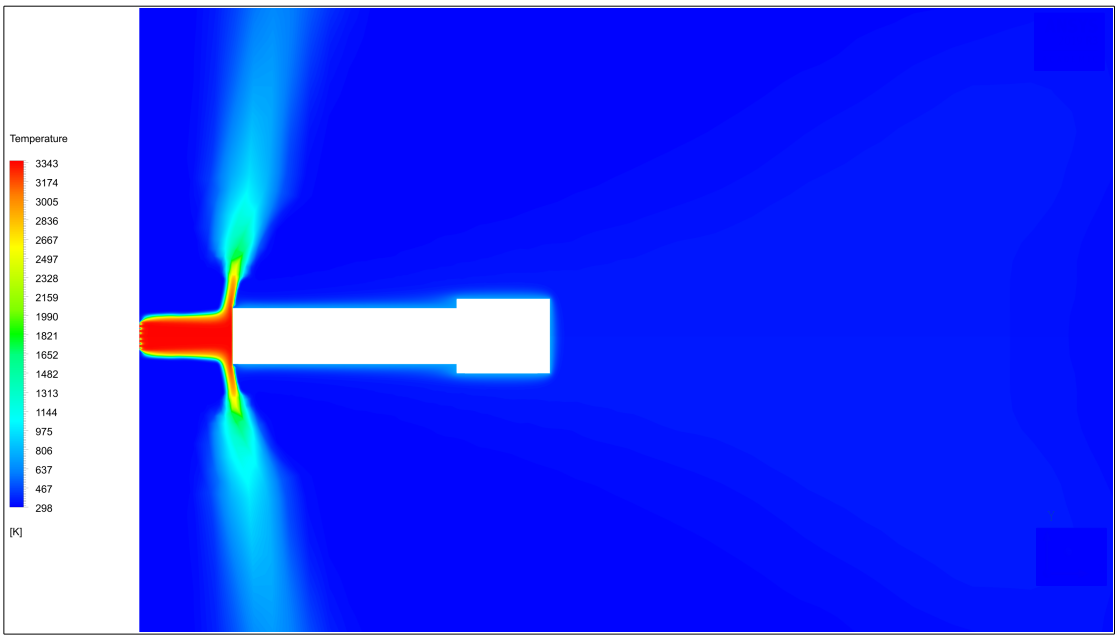

(a)

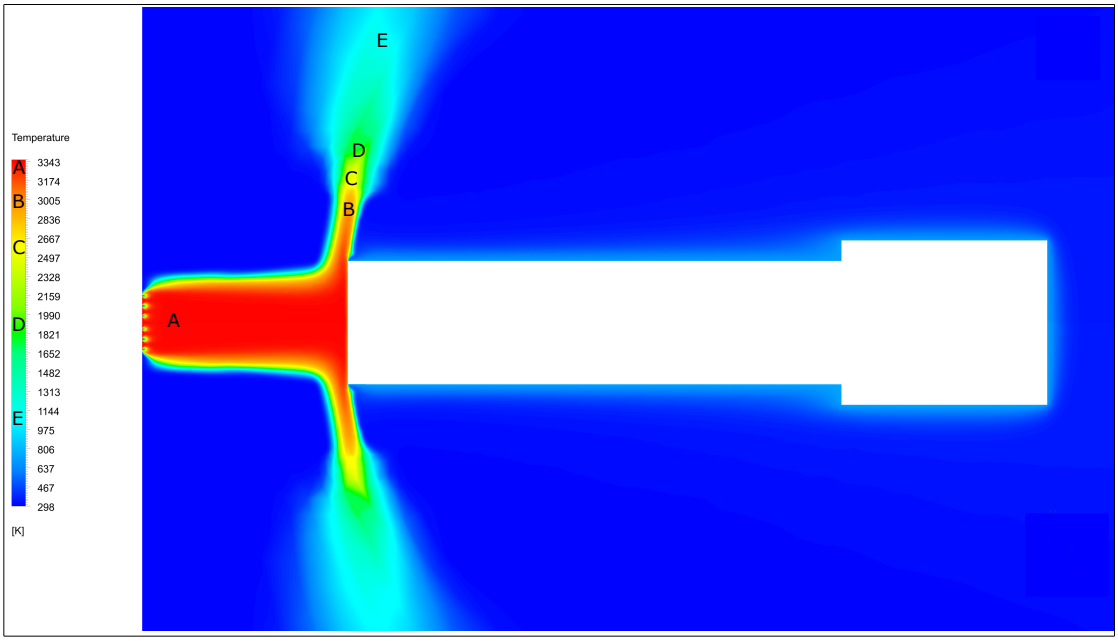

(b)

Figure 4.11: The temperature distribution of eddy dissipation concept model

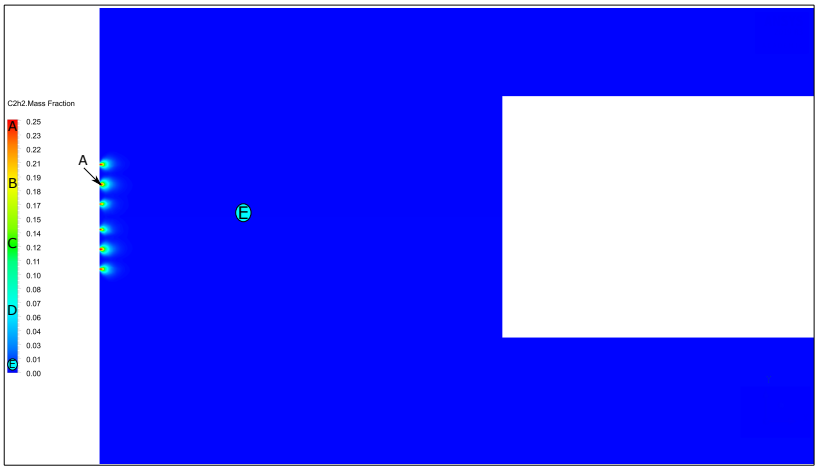

(a) Acetylene mass fraction

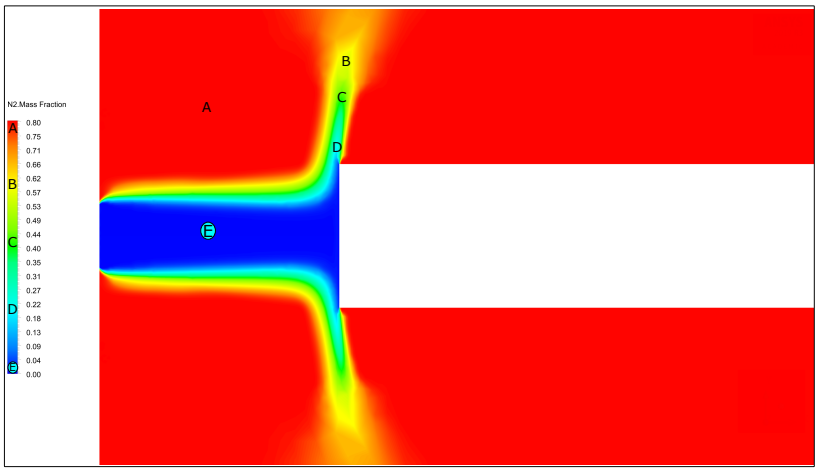

(b) Nitrogen mass fraction

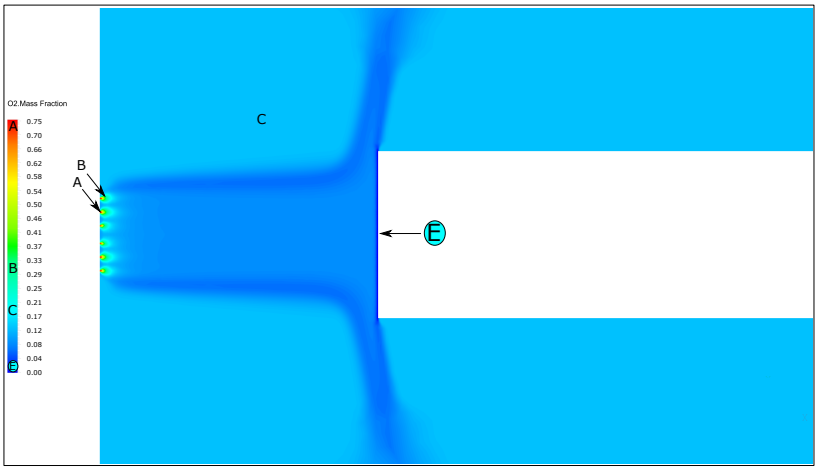

(c) Oxygen mass fraction

Figure 4.12: The mass factions of species in eddy dissipation concept model

The Figure 4.11 is the temperature field of the numerical solution of the eddy dissipation concept model. The maximum temperature is roughly 3343 K at the flame centre. It is obvious that using detailed chemical reaction and more accurate flow properties ensure more uniform flame structure in terms of temperature distribution. Besides, the flame with the eddy dissipation concept model is a bit thicker than the flame simulated with the eddy dissipation model as expected. The mass fraction of the acetylene in Figure 4.12a shows that the acetylene burns very fast due to interaction with oxygen whenever accessing to the solution domain. The local chemical composition is accurately computed, propending for a good estimation of the concentration of radicals and intermediate species, and a consequent proper and uniform the flame temperature fields.

Furthermore, the burner facility has been carried out with heat flux sensors at a distance of 50 mm to estimate overall heat fluxes over the front surface. The dimension of the front surface (0.15 mm) is being considered as same as sample material. The front boundary condition has been selected as *"Temperature"* about 718 K which is found from previous researches conducted at DLR [25]. The main of the investigation was targeting to get 2 MW/m^2 as it has been found in the aforementioned master thesis.

Table 4.14: Per cent variation of the overall heat flux at the sensor between numerical simulation and experimental measurements

	Boundary condition	Numerical Simulation (MW/m2)	Experimental measurement (MW/m2)	Variation
The heat flux sensor	T = 718 K	2.11	1.98	6.56

All in all, the eddy dissipation concept model with a detailed reaction mechanism performs accurate temperature and species formation relative to the eddy dissipation model.

As it is seen in Figure 4.13 and Table 4.15, the maximum pressure increases up to 245.15 MPa. This is directly relevant to using good flow properties for the oxyacetylene mixture. The pressure variation between numerical simulation and the experimental result decreases by half compared to the previous one and reaches a very good level which is around two per cent.

Table 4.15: The per cent variation between numerical simulation and experimental measurements of pressure quantity for the eddy dissipation concept model

Quantity	Numerical Simulation	Experimental Measurement	Variation (%)
Pressure at stagnation point (MPa)	245.15	240	2.14

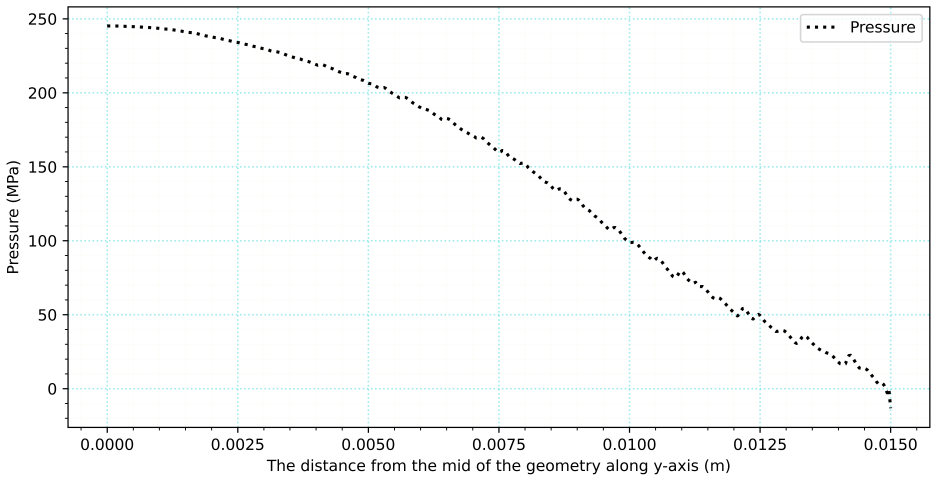

Figure 4.13: The pressure distribution of eddy dissipation concept model over the front surface

Consequently, the oxyacetylene flame has been generated with a very good species formation and a flow pattern which provides high accuracy estimations in terms of heat flux, pressure to investigate the thermal loads on the materials by the conjugate heat transfer.

4.4 Conjugate Heat Transfer

4.4.1 The Mesh Generation

The material dimensions and the zones can be seen in Figure 4.14. In Figure 4.14a, the dimensions are in terms of a millimetre. The copper holder will be designed with a water-cooled system while the graphite material is being considered without the cooling system at the backside.

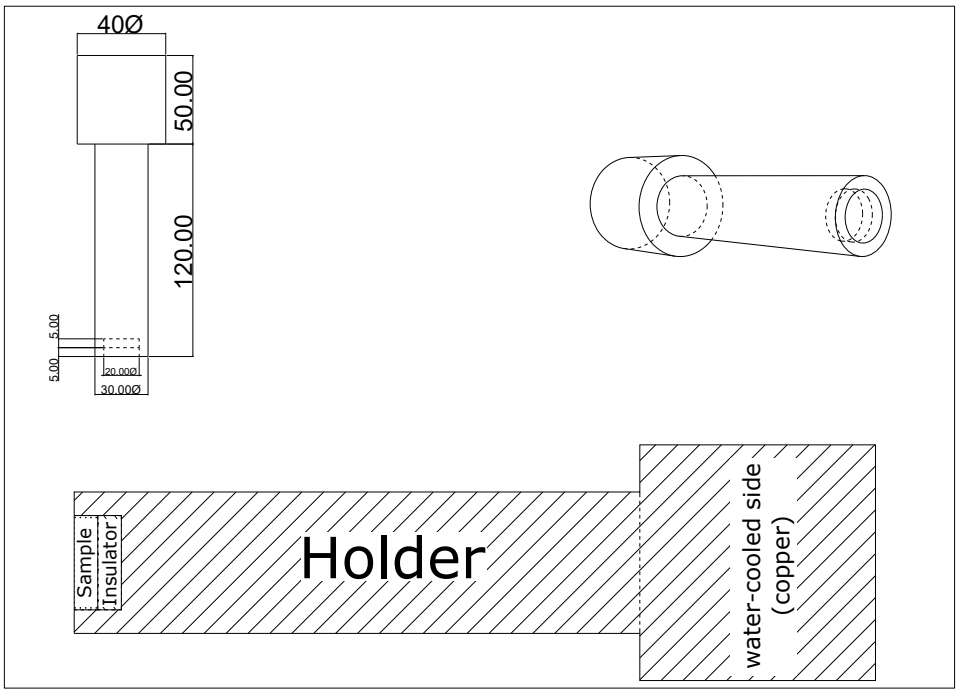

(a)

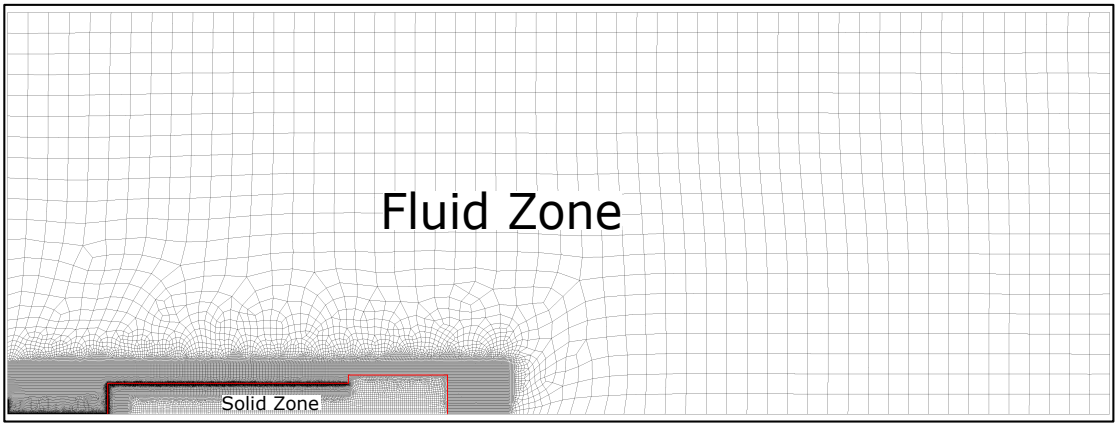

(b)

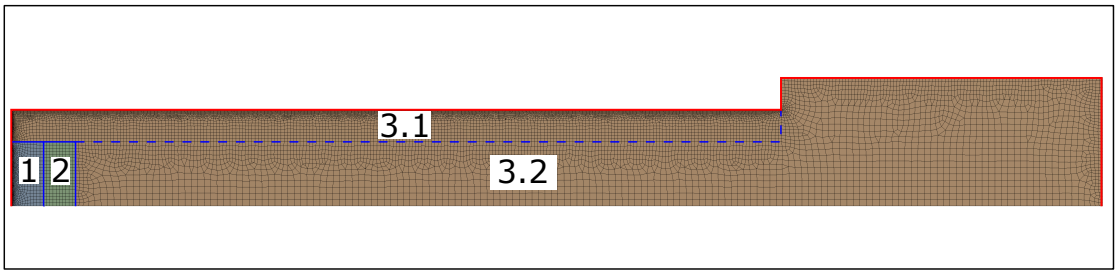

(c)

Figure 4.14: The material zones; (a) the dimensions of the solid body and the material zones; (b) the fluid and solid mesh zones; (c) the solid mesh zone

In the contact region labelled as the red line in Figure 4.14b, the conformal mesh is being used. The conformal mesh enables nodes to be matched with each other at the interface regions. This means that every node on one side of the interface can be matched with a node on the other side of the interface with a very low tolerance. In that way, additional interpolation caused by hanging nodes will not be required at the interface. This makes the computation faster and more accurate. The holder zone is divided into two pieces. The one separated with a blue dashed line (3.1) is a refined region. The cell sizes can be seen in Table 4.16.

Table 4.16: The mesh sizes inside the solid zone

Zone	**The mesh sizes (mm)**	**Number of elements (-)**
1	0.5	3491
2	0.5	200
3.1	0.5	9266
3.2	1	5795

4.4.2 Pre-processing

The test system is designed to evaluate thermal loads, such as temperature field and the heat flux, on materials heated by oxyacetylene flame. Hence, the numerical domain at this point composed of:

- fluid zone involving the oxyacetylene flame simulated with the eddy dissipation concept model
- a first solid body, high-temperature sample materials, such as CCSiC and UHT-CMC, using as thermal protection of spacecraft vehicles
- a second solid body, zirconium oxide (ZrO_2) fibrous ceramic using for insulation between sample material and holder
- a third solid body, water-cooled copper holder or graphite holder.

The thermal boundary conditions, the material properties for the solid bodies, and the corresponding emissivity values are reported in Table 4.17 and Table 4.18

Table 4.17: Solid zones thermal boundary conditions

Zone	**Boundary condition**	**Material**	**Emissivity**
Sample material	Coupled	CCSiC & UHT-CMC	0.85
Insulator	Coupled	ZrO_2	0.5
Holder (if cooled)	Coupled & $T = 295K$	Copper	0.5
Holder (without cooling)	Coupled	Graphite	0.9

The boundary condition specified as "coupled" indicates that the heat exchange between the oxyacetylene combustion and the solid is calculated by the software, accounting for conduction, convection, and radiation contributions. The boundary condition at the backside for the water-cooled copper holder is determined as 295 K.

Table 4.18: Thermal and physical properties of materials

Materials	**Specific heat capacity (J/kgK)**	**Thermal conductivity (W/mK)**	**Density (kg/m3)**
CCSiC	1800	9 (x-axis) 18 (y-axis)	1900
UHT-CMC	1200	22	4000
ZrO_2	753.624	0.5	1400
Copper	381	387.6	8978
Graphite	710	128	1920

Hypersonic and atmospheric re-entry vehicles experience temperatures above $2000K$ and encounter corrosive plasmas from the atmosphere at high speeds. The materials used in these vehicles, especially at the sharp edges, should maintain their shape under this severe oxidation, extreme heat fluxes and high mechanical stress conditions [1][2]. In this regard, carbon fibre reinforced silicon carbide matrix composite (CCSiC) and ultra-high temperature ceramic matrix composites (UHT-CMC) are being used in aerospace fields as thermal protection systems. The bulk materials for UHT-CMC are, for example, ZrB_2, HfB_2, HfC and TaC. These materials are developed to extend the application temperature of CMC to over $2000K$.

In the experimental facility, the zirconium oxide (ZrO_2) fibrous ceramic is used as an insulator material to protect the holder against the high thermal load. ZrO_2 has extremely low thermal conductivity and is designed for use to as high as 2000 °C and can be exposed to significantly higher temperatures (up to 2200 °C). Being dimensionally stable and reusable after many experiments makes it preferable for usage in the experiments as a very good insulator. On the other side, the holder has two concepts. The one is copper material with a water-cooled system at the backside while the other one is graphite which has a high emissivity and high conductivity property.

Table 4.19: Radiation model and angular discretization properties

Radiation model	
Model	Discrete ordinates (DO)
Theta divisions	5
Phi divisions	5
Theta pixels	3
Phi pixels	3
Flow iterations per radiation iteration	10
DO/Energy coupling	Off

The DO model has the properties named angular discretization. Theta divisions (N_θ) and Phi divisions (N_ϕ) determine the number of control angles used to discretize each octant of the angular space. Both of them are set to 2 as default. However, setting them 2 is considered as a coarse estimate. To get more reliable results, it is highly recommended to increase to a minimum of 3 or up to 5 [13]. On the other side, for problems involving symmetry, periodic, specular, or semi-transparent boundaries, a pixelation of 3×3 is recommended [13]. This will produce acceptable results. However, a finer angular discretization will be computationally expensive. Hence, the radiation equations should be solved every 10 iterations of energy equations.

4.4.3 Results

In Figure 4.15, the temperature fields of the materials placed at a distance of 50 mm from the burner are presented. The Figure 4.15a and Figure 4.15b show the result of CCSiC material with water-cooled copper and graphite holder respectively whereas the rests belong to UHT-CMC material. To better understand temperature variations inside the materials with changing distance, Figure 4.16 and Figure 4.17 is reported.

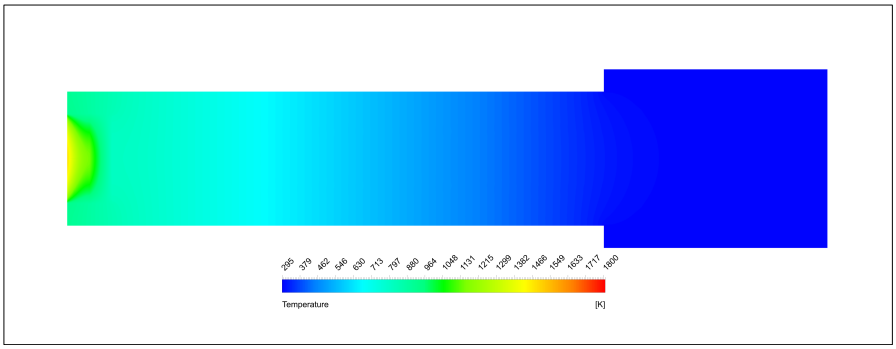

(a) CCSiC material with cooled-copper holder

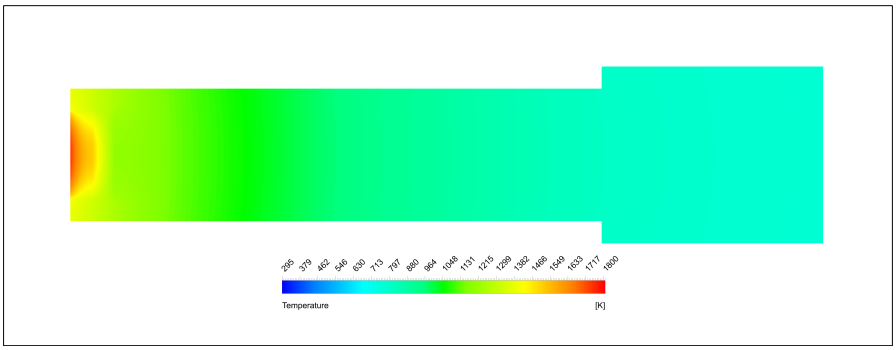

(b) CCSiC material with graphite holder

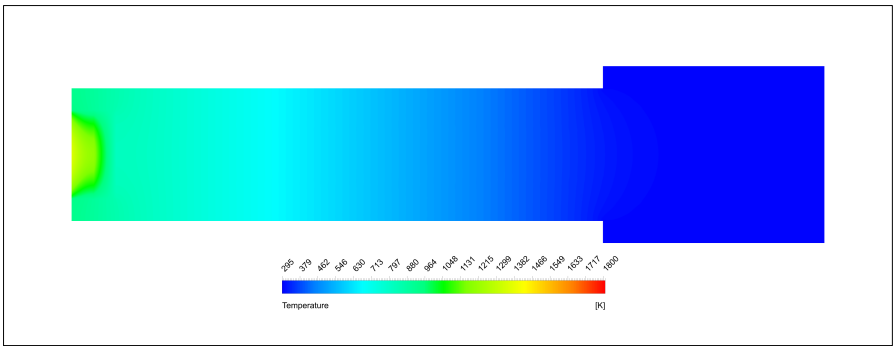

(c) UHT-CMC material with cooled-copper holder

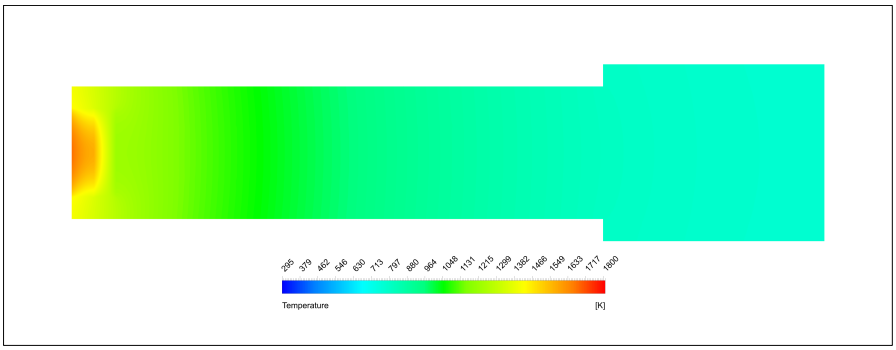

(d) UHT-CMC material with graphite holder

Figure 4.15: The temperature distribution of combustion simulation inside materials

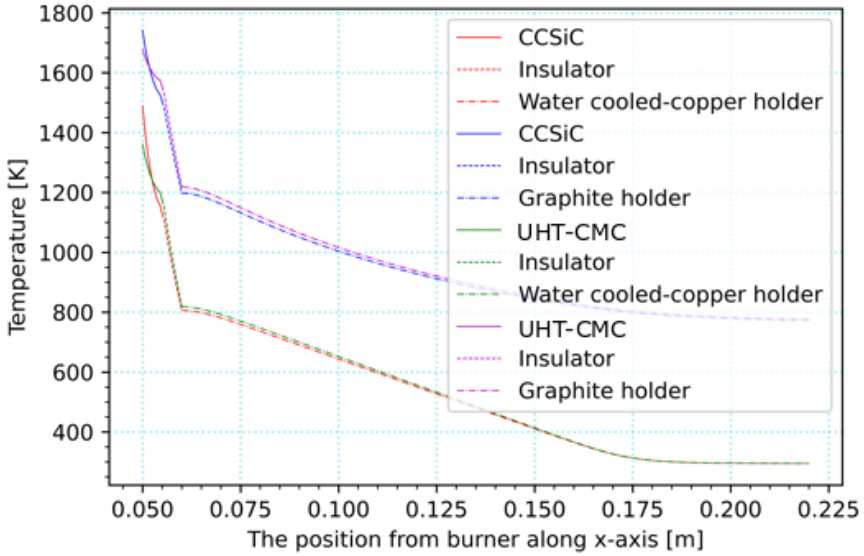

(a) The temperature distribution on the materials

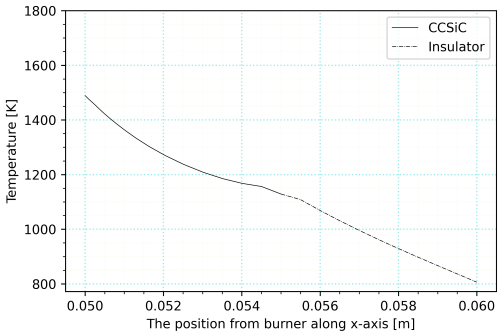

(b) CCSiC material with cooled copper holder

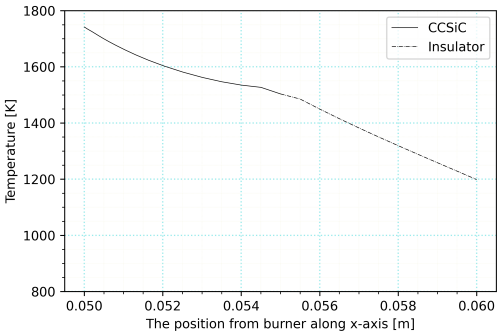

(c) CCSiC material with graphite holder

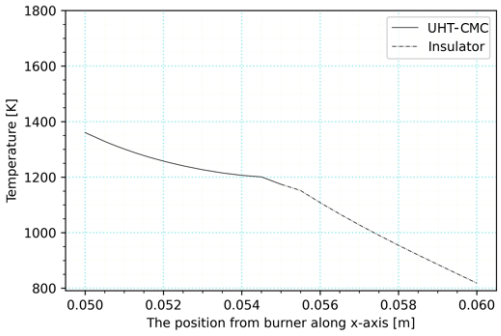

(d) UHT-CMC material with cooled copper holder

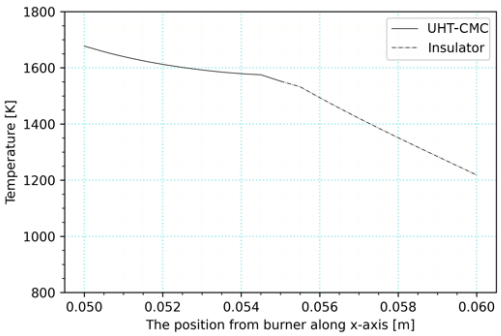

(e) UHT-CMC material with graphite holder

Figure 4.16: The temperature distribution inside materials along x-axis

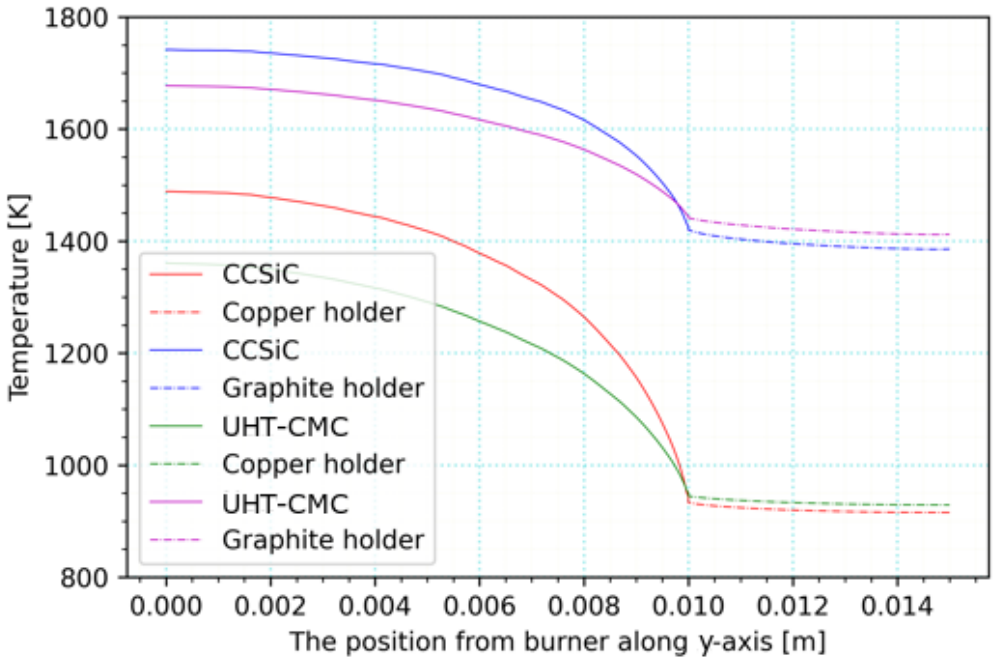

Figure 4.17: The temperature distribution over front surfaces of the material along y-axis

Figure 4.16 shows the temperature distribution inside materials along the x-axis. As remembered, the material is placed 50 mm from the burner. The graphite holder causes high temperatures in both sample materials as expected. The main reason is that graphites are super absorbent material with very high emissivity value. When Figure 4.17 is examined, it is understood that the front face of the graphite material is nearly 1.5 times hotter than the water-cooled copper materials. Therefore, the graphite material involving high temperature relatively causes the temperature rises on the sample materials. On the other hand, it is observed that the water-cooled copper material has a lower temperature field. As a result, both sample materials and the insulation material which are tested with a water-cooled copper holder are at a lower temperature.

Table 4.20: The temperature and heat flux quantities over the sample materials

Sample material	Holder type	The maximum temperature at stagnation point (K)	The overall heat flux over sample material (MW/m2)
CCSiC	Water cooled copper	1499	1.539
	Graphite	1741	1.000
UHT-CMC	Water cooled copper	1360	1.672
	Graphite	1677	1.087

The maximum temperature occurs at the mid of the sample materials on front surfaces where the first touch exists with the flame. CCSiC material has a relatively high specific heat capacity with very low density. Hence, the temperature at the front surface of CCSiC is higher than UHT-CMC material. However, in both figures (Figure 4.16 and Figure 4.17) shows that the temperature of UHT-CMC at the contact point of the sample material and insulator is higher than CCSiC material and further, the temperature decreases slower compared to CCSiC material. This is a direct consequence of having high thermal conductivity. The thermal load coming from front surface move faster inside UHT-CMC and make it hotter relatively.

The results indicate that the graphite holder is suitable for high-temperature experimental tests since it provides a higher thermal load on the sample material. However, the water-cooled copper material can be more appropriate for the successive experimental test due to comprising the less thermal load.

4.4.4 Verification of the Conjugate Heat Transfer Results

The heat transfer study estimated by combustion is a computationally very stiff system. Even if converged results are obtained at the end of combustion simulations, the simple case study which is without combustion will be generated in Ansys Fluent to check if the heat transfer results are correct or not.

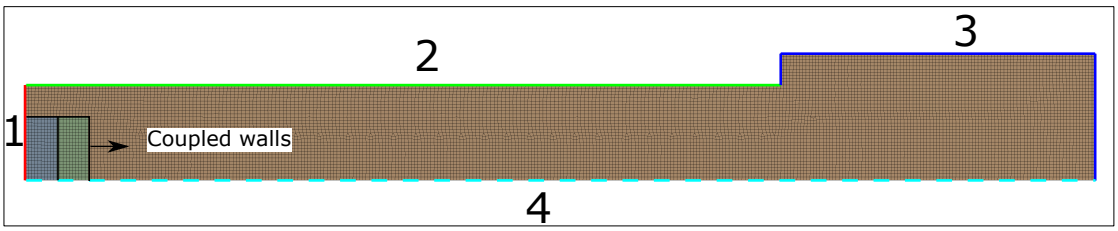

Figure 4.18: The mesh zone and the boundary conditions of the simple case study

Table 4.21: The boundary conditions for the simple case study

Boundary	Boundary condition	Defined properties
1	Mixed (convection and radiation)	Free stream temperature T = 3200 K Heat transfer coefficient = 1000 W/m2K Emissivities of materials
2	Radiation	Emissivities of materials
3	Radiation (graphite) Temperature (copper)	$\varepsilon = 0.9$ (graphite) T = 295 K (copper)
4	Axisymmetric	-

In Figure 4.18, the mesh zone of the simple case study can be seen. The system involves only a solid zone including materials. The minimum mesh size is determined as 2.5 mm for all zones.

The mixed boundary condition which makes the system enable to define convection and radiation heat transfer simultaneously on the front surface. The free stream temperature corresponds to the oxyacetylene flame temperature. Hence, it is determined as $3200K$. In the 3rd line, labelled with blue colour, the radiation heat transfer will be assigned for graphite while the temperature boundary conditions are being used for copper material. As it is remembered, the copper holder has been designed with the cooling system at the backside. The coupled walls inside the materials are set up with zero emissivity.

Table 4.22: The maximum temperature quantities obtained from the combustion and the simple case study simulations

Sample material	Holder type	The maximum temperature at the mid of material (K) (combustion simulation)	The maximum temperature at the mid of material (K) (simple case study)	Variation (%)
CCSiC	Water cooled copper	1499	1500	0.06
	Graphite	1741	1756	0.85
UHT-CMC	Water cooled copper	1360	1379	1.37
	Graphite	1677	1689	0.71

Table 4.23: The total heat flux quantities obtained from the combustion and the simple case study simulations

Sample material	Holder type	The total heat flux over the front surface (W/m2K) (combustion simulation)	The total heat flux over the front surface (W/m2K) (simple case study)	Variation (%)
CCSiC	Water cooled copper	1.535	1.539	0..23
	Graphite	0.987	1.000	1.28
UHT-CMC	Water cooled copper	1.676	1.672	0.24
	Graphite	1.095	1.087	0.75

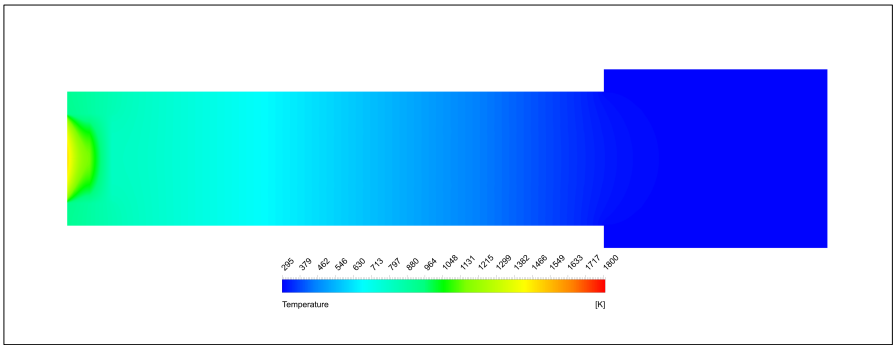

(a) CCSiC material with cooled-copper holder

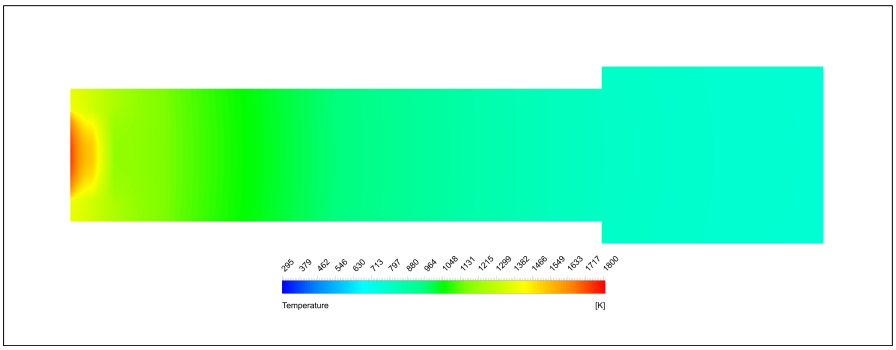

(b) CCSiC material with graphite holder

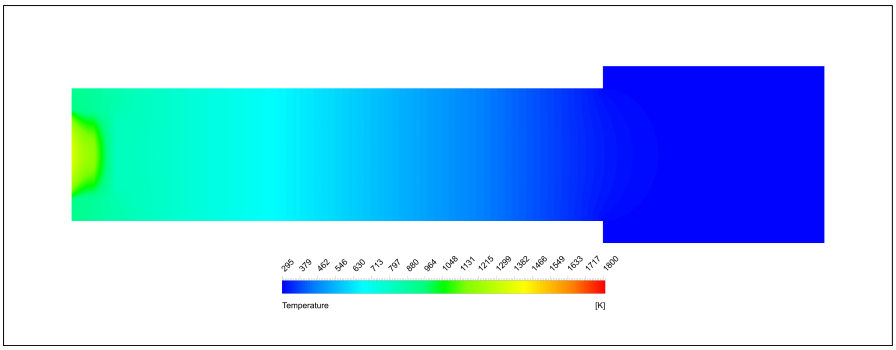

(c) UHT-CMC material with cooled-copper holder

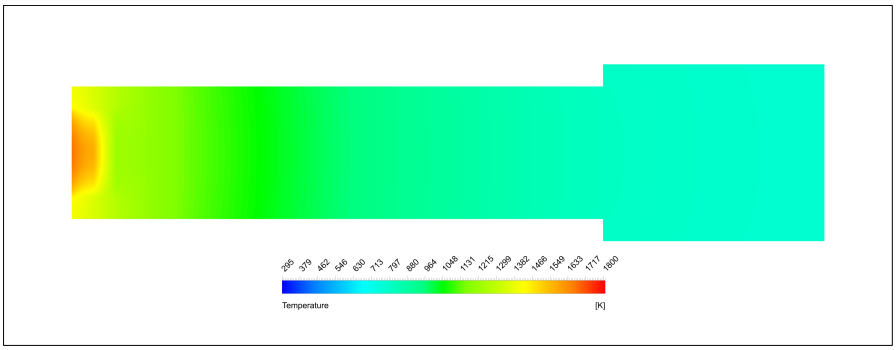

(d) UHT-CMC material with graphite holder

Figure 4.19: The temperature distribution of the simple case study inside materials

The Figure 4.15 and Figure 4.19 shows exactly the same characteristics. The Table 4.22 and Table 4.23 indicates variation between combustion simulations and the simplified case study simulations in terms of the maximum temperature at the mid of the sample material and the total heat flux over the front surface. The results confirm that the numerical simulations of the heat transfer obtained from combustion model match with the numerical simulations of the simplified case study. A very good agreement (with differences below 10 per cent) was found between simplified and combustion simulation models, encouraging further activity for the experiments.

Chapter 5

Summary and Conclusion

5.1 Summary

The main task of the thesis was the characterization of the acetylene-oxygen combustion, evaluation of the temperature fields and heat flux density acting on sample materials with the help of numerical simulations using Ansys Fluent. The simulations then led to the design of a general concept for sample holder.

The numerical simulation of the combustion systems is computationally very stiff. Hence, the step by step solution method from cold flow to conjugate heat transfer was found as a very useful procedure to ensure a stable solution in terms of convergence properties. It is a well-known fact that the accuracy of a CFD simulation, Reynold Averaged Numerical Simulations (RANS) is applied, is mainly determined by the mesh resolution and the turbulence model. In this regard, high-quality unstructured quad-dominant mesh with triangle elements in the transition areas between fine and coarse mesh zones has been generated. The SST k-omega turbulence model has been selected due to providing high accuracy at the regions where the high gradients and flow separations exist. In the first step, called cold flow generation, the velocity has been found zero at the stagnation point where the pressure is in its maximum. Further, numerical and experimental results in terms of pressure quantity at the stagnation point were close to each other with 0.47 per cent variation. Consequently, the basic cold flow pattern which is modelled with a high degree of accuracy has provided good initial condition for the combustion simulations.

The eddy-dissipation concept model utilised with detailed chemical reaction mechanisms has been found as a good model for the generation of accurate oxyacetylene flame.

The multi-step detailed reaction mechanisms have been implemented from the popular article of Charles Westbrook and Frederick Dryer written about *"Simplified reaction mechanisms for the oxidation of hydrocarbon fuels in flames"*. These mechanisms having 12 species combines 21 elementary reactions involving the global reaction mechanism and the $H_2 - O_2 - CO$ mechanisms [16]. The flow properties are also critical to estimate the proper formation of the flame. The ideal gas assumption was used since most species, e.g., oxygen, nitrogen, and carbon dioxides, behave like an ideal gas in high temperatures. The kinetic theory as another important flow property which explains the transport properties of the particles, such as mass diffusivity, was used. Further, it is strongly recommended to apply kinetic theory for the estimation of thermal conductivity and viscosity of all species. In this way, the kinetic energy which is strictly thermal due to particular interactions, such as molecular collisions, was better modelled. The computational costs are proportional to N^2 where N is the number of species. Hence, the coarse solution should be considered and performed before the eddy dissipation concept model applied. In this sense, the single-step more product concept has been utilized with coarse flow properties. The reaction mechanism consisting of one global reaction and 10 species has been generated by the NASA Chemical Equilibrium Applications software. The flow was considered as incompressible ideal gas flow and then the default constants offered by Ansys Fluent were applied for mass diffusivity, thermal conductivity and viscosity rather than kinetic theory. The initial solution provided by the eddy dissipation model significantly reduced the computational time and instabilities of the equations to be solved for the eddy dissipation concept model. As a result, the flame has been characterized with good species formations and thermal flow pattern to investigate the thermal loads on the sample materials located at a distance of 50 mm by the conjugate heat transfer.

5.2 Conclusion

High-temperature materials, e.g., CCSiC material developed at German Aerospace Center and UHT-CMC material, are numerically tested with two different types of the holder which are water-cooled copper and graphite. Additionally, in the experimental facility, the ZrO_2 (zirconium oxide) fibrous ceramic has been placed between sample material and holder to reduce the thermal load on the holder material. The numerical investigations indicate that the insulator material (ZrO_2) which has extremely low thermal conductivity absorb thermal loads and reduces the temperature of the holder material remarkably. The maximum temperature of the CCSiC and UHT-CMC materials at the front surfaces for the graphite holder was 1741 K, 1677 K respectively while the temperature for the water-cooled copper holder was

found 1499 K, 1360 K respectively. Hence, the graphite holder can be considered when the sample materials are needed to be exposed to high temperature whereas the water-cooled copper holder is more appropriate for successive experimental tests due to involving less thermal load.

As a result, it is mentioned that the materials used for thermal protection in hypersonic vehicles are wanted for application at temperatures over 2000 K according to given statements in the introduction. However, numerical simulations found the maximum temperatures to be expected at 1741 K which is less than 2000 K. So the results can be evaluated in two senses as follow:

- One of the main goals of the experiments is to have uniform heating over the whole sample materials. It is seen that the setup produces quite nice homogeneous temperature fields on the sample surface up to 1741 K so there is certainly the potential to do good quality testing.
- The temperatures are not as high as it would be desired to test for the aforementioned applications at very high temperatures.

In light of the given points above, some further studies can still be made. The main aim of further research should be based on maintaining the uniformity of the temperature fields and seeking to increase the test temperatures. Due to the complexity of successive simulations and inadequacy of time, they have been left for the future. In this regard, some interesting activities, that are worth investigating further, are given as follows:

- The temperature acting on the sample material can be increased by changing the distance the materials are deployed. Therefore, simulations should be tried at different distances before the next suggestions.
- Other types of the burners, e.g., single hole burners, can be investigated rather than multi-hole burners. Some researchers who use single-hole burners with a very small impingement area achieved much higher temperatures [1][2][3].
- Besides, the simulations can be tried with different gas parameters, e.g., the flow rates and mixture ratio.

However, this should be noted that the significant computational cost of the model (the one configuration require about 50 000 iterations to get convergence, with approximately 2 days with 24/7 operation time) highlights the necessity of the time frame arrangements to enhance the usefulness of the fluid-dynamic outputs in further academic studies.

Appendices

Appendix A

NASA Chemical Equilibrium with Applications (CEA)

A.1 The purpose of the NASA CEA

"The NASA Computer program CEA (Chemical Equilibrium with Applications) estimates chemical equilibrium compositions and properties of complex mixtures. Applications include assigned thermodynamic states, theoretical rocket performance, Chapman-Jouguet detonations, and shock-tube parameters for incident and reflected shocks. CEA represents the latest in a number of computer programs that have been developed at the NASA Lewis (now Glenn) Research Center during the last 45 years. These programs have changed over the years to include additional techniques. Associated with the program are independent databases with transport and thermodynamic properties of individual species. Over 2000 species are contained in the thermodynamic database. The program is written in ANSI standard FORTRAN by Bonnie J. McBride and Sanford Gordon. It is in wide use by the aerodynamics and thermodynamics community, with over 2000 copies in distribution." [15]

A.1.1 The capabilities of the NASA CEA

Several problem types can be defined in NASA CEA.

Assigned Temperature and Pressure (tp):

Chemical equilibrium composition and properties are measured for preferred temperatures and pressures.

Combustion (Enthalpy and Pressure) (hp):

Enthalpy possessed constant occurring in adiabatic flame temperature, equilibrium mixture properties and composition.

Assigned temperatures and volumes (tv):

Chemical equilibrium composition and properties are accounted for prescribed temperatures and a set of either specified specific volumes or densities.

Combustion (Internal energy and volumes) (uv):

Chemical equilibrium composition and properties are determined for specified internal energies and detailed total reactant specific volumes or densities.

Rocket (rkt):

Theoretical rocket performance parameters can be estimated for:

- infinite-area or finite-area combustors
- chemical equilibrium for all points or freeze composition after combustion, throat, or any exit point
- thermal transport properties

Shock tube (shock):

Shock properties in terms of prescribed velocities are estimated.

Chapman-Jouquet detonation (det):

Chapman-Jouguet detonation properties are assessed for unburned gaseous reactants at specified temperatures and pressures.

Assigned entropy and pressures (sp):

Converges on both the gaseous and concentrated products for a reactant mixture with a specified entropy and pressures.

Assigned entropy and either specific volumes or densities (sv):

Chemical equilibrium composition and properties are assessed for detailed entropy and each specified total reactant specific volume or density.

A.1.2 The calculation of stoichiometric coefficients for oxyacetylene combustion

As it is known that the single-step more product concept reaction mechanism has been generated by NASA CEA software. The generation procedure will be investigated step by step. First of all the problem type should be selected as a rocket. Because the infinite area combustor under equilibrium condition will be used for the generation of the reaction.

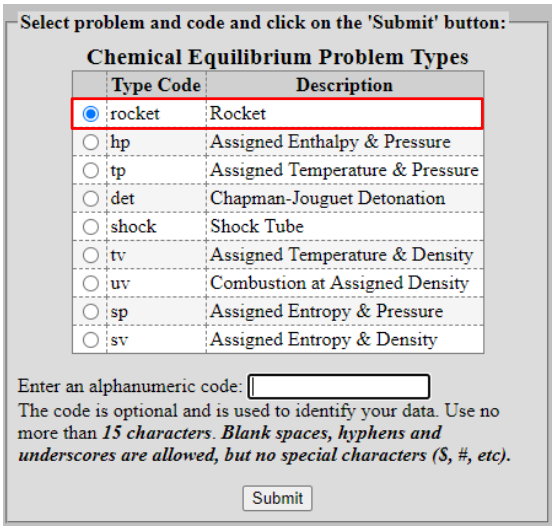

Figure A.1: The problem types in NASA CEA

The following properties should be defined for obtaining exact combustion products:

- pressure (ideally 1 atm)
- fuel (acetylene)
- oxidizer (oxygen)
- oxid/fuel ratio (percentage of fuel: 25)

The oxid/fuel ratio is selected as "%Fuel by Weight" in the model dialogue box. 25 per cent will provide a stoichiometric condition for oxyacetylene reactions.

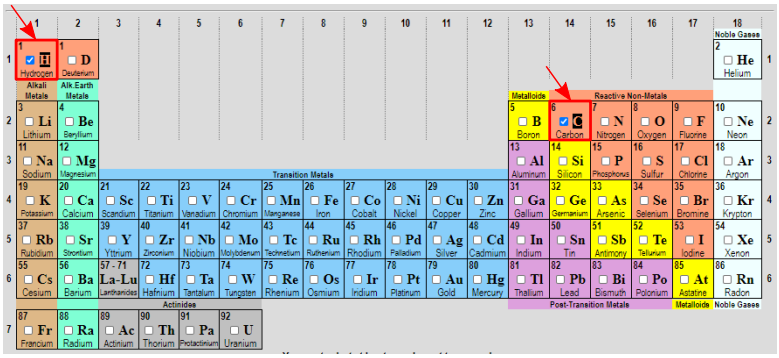

Figure A.2: The periodic table presented in NASA CEA

The acetylene is not included in the species list. Therefore, the periodic table in the Figure A.2 should be used to select acetylene. To do so, carbon and hydrogen atoms are selected and afterwards, the acetylene will be activated for selection in the new opening window.

The mass fractions concerning product species of the reaction can be seen in the Figure A.3. The green column represents the mass fraction of species in the injector face while the blue one corresponds to exit conditions. Each mass fraction should be converted to stoichiometric coefficients for implementing into ANSYS Fluent.

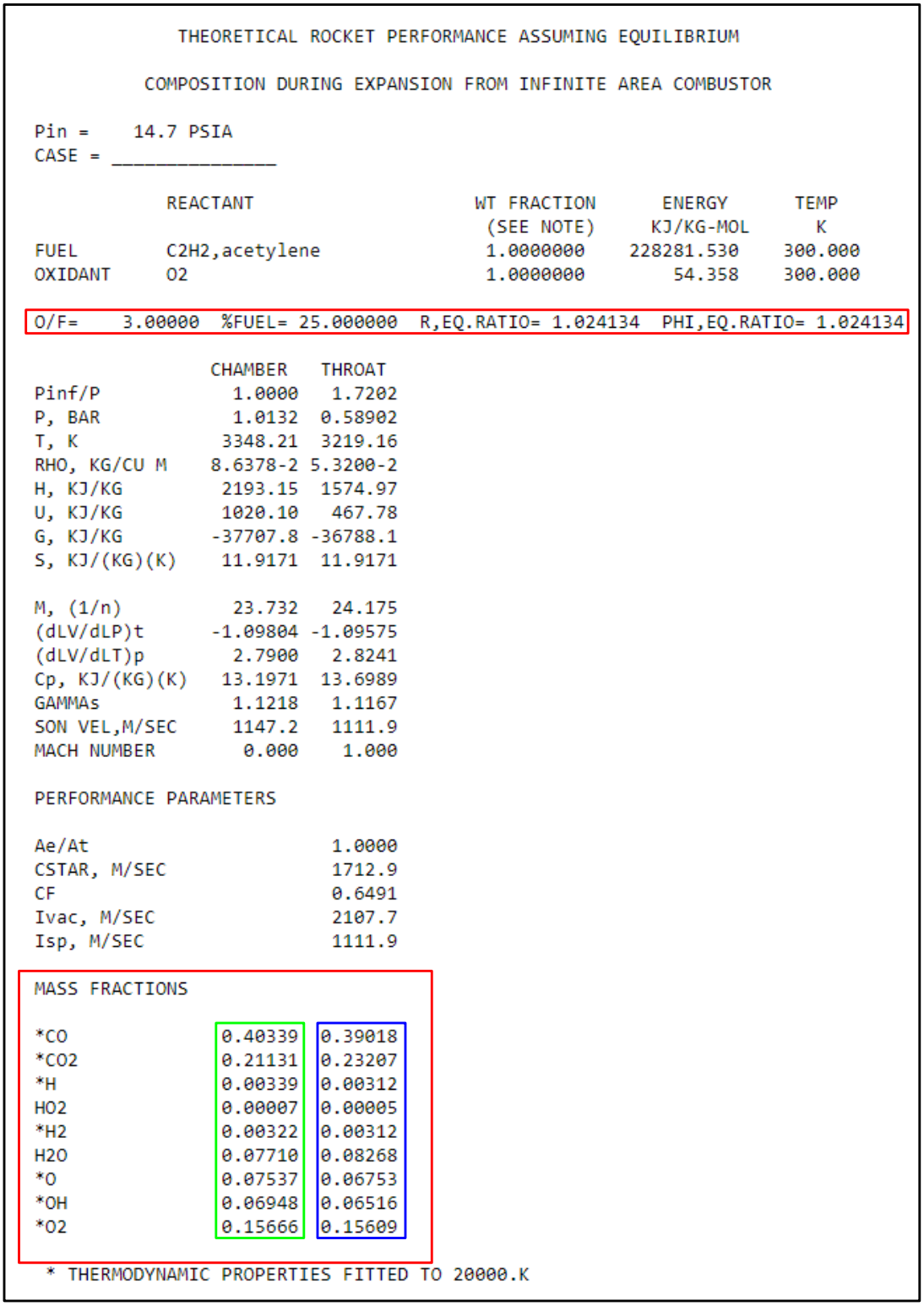

```
            THEORETICAL ROCKET PERFORMANCE ASSUMING EQUILIBRIUM

          COMPOSITION DURING EXPANSION FROM INFINITE AREA COMBUSTOR

Pin =    14.7 PSIA
CASE = _______________

            REACTANT                    WT FRACTION      ENERGY      TEMP
                                         (SEE NOTE)     KJ/KG-MOL      K
FUEL        C2H2,acetylene               1.0000000    228281.530    300.000
OXIDANT     O2                           1.0000000        54.358    300.000

O/F=    3.00000  %FUEL= 25.000000  R,EQ.RATIO= 1.024134  PHI,EQ.RATIO= 1.024134

                CHAMBER   THROAT
Pinf/P            1.0000   1.7202
P, BAR            1.0132  0.58902
T, K             3348.21  3219.16
RHO, KG/CU M    8.6378-2 5.3200-2
H, KJ/KG         2193.15  1574.97
U, KJ/KG         1020.10   467.78
G, KJ/KG        -37707.8 -36788.1
S, KJ/(KG)(K)    11.9171  11.9171

M, (1/n)          23.732   24.175
(dLV/dLP)t      -1.09804 -1.09575
(dLV/dLT)p        2.7900   2.8241
Cp, KJ/(KG)(K)   13.1971  13.6989
GAMMAs            1.1218   1.1167
SON VEL,M/SEC     1147.2   1111.9
MACH NUMBER        0.000    1.000

PERFORMANCE PARAMETERS

Ae/At                      1.0000
CSTAR, M/SEC               1712.9
CF                         0.6491
Ivac, M/SEC                2107.7
Isp, M/SEC                 1111.9

MASS FRACTIONS

*CO             0.40339  0.39018
*CO2            0.21131  0.23207
*H              0.00339  0.00312
HO2             0.00007  0.00005
*H2             0.00322  0.00312
H2O             0.07710  0.08268
*O              0.07537  0.06753
*OH             0.06948  0.06516
*O2             0.15666  0.15609

  * THERMODYNAMIC PROPERTIES FITTED TO 20000.K
```

Figure A.3: The species and the mass fractions of oxyacetylen flame calculated in NASA CEA

Bibliography

[1] Anish Paul et al. "UHTC composites for hypersonic applications". In: (2012).

[2] A Paul et al. "UHTC–carbon fibre composites: Preparation, oxyacetylene torch testing and characterisation". In: *Journal of the European Ceramic Society* 33.2 (2013), pp. 423–432.

[3] Carmen Carney et al. "Qualitative analysis of hafnium diboride based ultra high temperature ceramics under oxyacetylene torch testing at temperatures above 2100 C". In: *Journal of the European Ceramic Society* 34.5 (2014), pp. 1045–1051.

[4] David E Glass et al. "Testing of DLR C/C-SiC and C/C for HIFiRE 8 scramjet combustor". In: *19th AIAA International Space Planes and Hypersonic Systems and Technologies Conference*. 2014, p. 3089.

[5] Henk Kaarle Versteeg and Weeratunge Malalasekera. *An introduction to computational fluid dynamics, the finite volume method*. Pearson education, 2007.

[6] Nancy Hall. *Navier-Stokes equations 3 - dimesional - unsteady*. 2005. URL: `https://www.grc.nasa.gov/www/k-12/airplane/nseqs.html`.

[7] Philip G Drazin and Norman Riley. *The Navier-Stokes equations: a classification of flows and exact solutions*. London Mathematical Society Lecture Note Series 334. Cambridge University Press, 2006.

[8] Giancarlo Alfonsi. "Reynolds-averaged Navier–Stokes equations for turbulence modeling". In: *Applied Mechanics Reviews* 62.4 (2009).

[9] TJ Chung. *Computational fluid dynamics*. Cambridge university press, 2010, pp. 6–11.

[10] Fadl Moukalled, L Mangani, Marwan Darwish, et al. *The finite volume method in computational fluid dynamics*. Vol. 6. Springer, 2016, pp. 6–11.

[11] David C Wilcox et al. *Turbulence modeling for CFD*. Vol. 2. DCW industries La Canada, CA, 1998.

[12] Jonas Bredberg. "On the wall boundary condition for turbulence models". In: *Chalmers University of Technology, Department of Thermo and Fluid Dynamics. Internal Report 00/4. G oteborg* (2000), pp. 8–16.

[13] INC Ansys. "ANSYS FLUENT user's guide". In: *Canonsburg, PA* (2011).

[14] Francis Westley. *Table of recommended rate constants for chemical reactions occurring in combustion*. Tech. rep. National Standard Reference Data System, 1980.

[15] Christopher Snyder. *Chemical Equilibrium with Applications Online*. 2018. URL: `https://www.grc.nasa.gov/WWW/CEAWeb/ceaHome.htm`.

[16] Charles K Westbrook and Frederick L Dryer. "Simplified reaction mechanisms for the oxidation of hydrocarbon fuels in flames". In: *Combustion science and technology* 27.1-2 (1981), pp. 31–43.

[17] Daniel J Jacob. *Introduction to atmospheric chemistry*. Princeton University Press, 1999, p. 155.

[18] Mehdi Bidabadi, Ali Haghiri, and Alireza Rahbari. "The effect of Lewis and Damköhler numbers on the flame propagation through micro-organic dust particles". In: *International Journal of Thermal Sciences* 49.3 (2010), pp. 534–542.

[19] Yunus A Cengel and Michael A Boles. *Thermodynamics: An Engineering Approach 8th Editon (SI Units)*. The McGraw-Hill Companies, Inc., New York, 2015.

[20] Theodore L Bergman et al. *Fundamentals of heat and mass transfer*. John Wiley & Sons, 2011.

[21] *Wikipedia, Electromagnetic spectrum*. URL: `https://commons.wikimedia.org/wiki/File:Electromagnetic-Spectrum.svg`.

[22] E. M. Greitzer and Z. S. Spakovszky ans I. A. Waitz. *Heat transfer by thermal radiation*. URL: `https://web.mit.edu/16.unified/www/FALL/thermodynamics/notes/node133.html`.

[23] Michael F Modest. *Radiative heat transfer, Second Edition*. Academic press, 2013.

[24] Jörg Franke and Alexander Baklanov. *Best practice guideline for the CFD simulation of flows*. Cost, 2007.

[25] Jakob Rieser. "Design of a probe for determining the heat flux density in an oxy-acetylene flame". MA thesis. Stuttgart: German Aerospace Center, 2009.

[26] F Marra et al. “Numerical simulation of oxy-acetylene testing procedure of ablative materials for re-entry space vehicles”. In: *Proceedings of the Institution of Mechanical Engineers, Part L: Journal of Materials: Design and Applications* 225.1 (2011), pp. 32–40.